# The Atmospheric Effects Model (AEM): Numerical estimations of asteroid survivability for crater formation on Venus, Earth, and Mars

**M. J. Hughes[1], R S. McGary[2], T. M. Pavelsky[1], and R. D. Mills[1]**

[1]University of North Carolina at Chapel Hill, Chapel Hill, NC
[2]James Madison University, Harrisonburg, VA

**Key Points:**

- We developed a modular MATLAB script to estimate projectile evolution through an atmosphere and produce a corresponding crater population.
- Decades of numerical atmospheric effect equations, assumptions, and parameters were synthesized, compared, and optimized for model runs.
- Projectile masses required for crater formation >1 km are at least $10^6$ kg for Mars, $10^8$ kg for Earth, and $10^{10}$ kg for Venus.

Corresponding author: M. J. Hughes, `mjdudek@email.unc.edu`

**Abstract**

The extent to which a planet's atmosphere filters incoming projectiles impacting its surface influences the primary crater population, offering insights into a planet's surface age and evolution. The Atmospheric Effects Model (AEM) is a user-friendly tool to study the evolution of projectiles (asteroids and meteoroids) through an atmosphere, approximating impact crater formation likelihood and characteristics. By synthesizing decades of numerical methodologies into a cohesive, modular code, we enable the community to easily test various equations and assumptions when estimating projectile behavior in an atmosphere. Using AEM, we assess the effects of deceleration, mass loss, and fragmentation on a theoretical projectile population through Venus, Earth, and Mars atmospheres. Projectiles span a range of densities (2,700 – 7,800 kg/m$^3$), diameters (1 m – 10 km), velocities (1 – 40 km/s), and trajectory angles (15° – 90° relative to horizontal). We optimize model equations and assumptions using known terrestrial impacts (Chicxulub and Meteor Crater) and observed meteor phenomena (Tunguska airburst and Chelyabinsk bolide). Atmospheric filtration of small projectiles is sensitive to atmospheric characteristics (density and pressure). Variations in equations and assumptions yield reasonable results when applied correctly. Model results indicate that projectiles creating craters $\geq$ 1 km in diameter require initial masses $\geq 10^6$ kg for Mars, $10^8$ kg for Earth, and $10^{10}$ kg for Venus. Applications for AEM include constraints on planetary surface ages and assessments of analytical errors in cratering models.

## Plain Language Summary

A planet's atmosphere can filter and prevent projectiles (asteroids and meteoroids) from striking the surface to form craters, with denser atmospheres filtering more projectiles than less dense atmospheres. This extent of filtering directly affects the potential size and frequency of primary crater formation. This relationship between atmospheric density and impactor populations can help us figure out how a planet's surface has changed over time. The Atmospheric Effects Model (AEM) described here is a modular tool to investigate the evolution of projectile characteristics through an atmosphere to approximate the likelihood of crater formation. Using AEM, we examine the effects of deceleration, mass loss, and fragmentation on projectile populations through the atmospheres of Venus, Earth, and Mars. We show that planetary atmospheres effectively filter small projectiles and that variations in algorithms and parameters produce reasonable results when applied correctly. Model results show that projectiles required to produce a crater at least 1 km in diameter have initial masses at least $10^6$ kg for Mars, $10^8$ kg for Earth, and $10^{10}$ kg for Venus. AEM can be used in future studies to approximate asteroid survival through atmospheres to constrain surface age and can allow analytical error in methodologies to be quantified and compared.

## 1 Introduction

Impact craters are among the most prevalent geologic features in the solar system and can be found on nearly all terrestrial planets, satellites, and asteroids. The flux of impactors themselves (i.e., asteroids, meteoroids, and comets) has evolved in conjunction with the formation of our solar system, with large impacts occurring frequently early in the solar system's formation as planetesimals collided, accreted, and differentiated into proto-planets. Eventually, these planets gathered enough material to clear their orbital paths of all other major bodies (Stevenson, 1987). This clearing process resulted directly in the reduction of the magnitude and frequency of impacts to the larger bodies over time. This feature of impact cratering has allowed researchers to relatively date a planet's surface based on its crater size-frequency distribution (CSFD) (Holsapple, 1993; Neukum et al., 2001; Stoffler, 2006), with older surfaces generally having larger overlapping craters (e.g., Lunar Highlands) and younger surfaces having smaller and more dispersed craters

(e.g., Lunar mare) (Neukum et al., 2001; Stoffler, 2006). Examinations of craters can also inform us of surface and subsurface processes by the varying degrees of weathering, erosion, and tectonic activity (Phillips et al., 1992; Michel & Morbidelli, 2007; Fassett, 2016). Thus, the combination of crater frequency and morphology on a planetary surface can constrain its age and geologic history.

However, because planetary atmospheres can cause deceleration, mass loss, and fragmentation of incoming projectiles, the size of a crater produced at impact can vary depending on the extent of atmospheric effects on the projectile (Baldwin & Sheaffer, 1971; Schultz, 1992; Bland & Artemieva, 2003). For example, a projectile with the same physical and initial characteristics would form a larger crater on a planetary body with no atmosphere than on a planet with an atmosphere - assuming all other things are equal. Therefore, having constraints on the projectile characteristics (i.e., mass, velocity, and angle of trajectory), that can "survive" (i.e., withstand) a target's atmosphere provides insights into the possible projectile populations that formed the distribution(s) of craters that we see today (Neukum et al., 2001; Michel & Morbidelli, 2007). For these reasons, accurately estimating the evolution of projectiles through a planet's atmosphere is crucial for understanding the impactor population and approximating the time of crater formation.

The current methods for modeling atmospheric effects on projectiles include numerical techniques, which incorporate empirical relationships (Baldwin & Sheaffer, 1971; Passey & Melosh, 1980; Collins et al., 2005; Melosh, 2011), and hydrodynamical techniques, which incorporate laws of fluid flow (Ivanov et al., 1997; V. V. Shuvalov et al., 1999; V. Shuvalov, 1999; Artemieva & Shuvalov, 2001; Korycansky et al., 2000). Many modeling methodologies are computationally intensive in runtime and memory allocation. To date, there are currently no numerical models that approximate the extent of atmospheric filtering on a custom projectile population to multiple planetary targets or models that can easily switch between and compare methodological equations and assumptions from several decades of literature on the topic.

The mechanical Atmospheric Effects Model (AEM) developed in this study was built in MATLAB to calculate the evolution of a projectile population's altitude, angle of trajectory, mass, velocity, and fragmentation during its passage through a planet's atmosphere and to approximate the relative crater population produced. AEM synthesizes decades of mechanical atmospheric effect methodologies into a single code that can be modified for future studies into projectile evolution through any planetary atmosphere. In this study, AEM is assessed through 1) varying atmospheric effect equations and assumptions, 2) employing observationally constrained characteristics of impactors to ground-truth projectile evolution through Earth's atmosphere and terrestrial crater formation, and 3) applying a theoretical projectile population to the surfaces of the Moon, Mars, Earth, and Venus to evaluate projectile survivability under a range of atmospheric conditions and individual projectile characteristics.

## 2 Review of Modeling Atmospheric Effects

The atmospheric effect on meteors is a relatively intuitive but mechanically complex topic. We have meteor sightings dating back centuries (Vogel, 2020), and high-resolution observations of recent meteor phenomena (Borovicka et al., 2013). These observations have influenced how this complex process can be modeled. Observations of meteor flight in Earth's atmosphere, meteorite strength and composition measurements, along with lab experiments on hypervelocity projectiles, have provided an in-depth look at the interactions between a projectile and our atmosphere. A projectile traveling through Earth's atmosphere is minimally affected above an altitude of 80 km, below which the outer surface of the asteroid/meteor is slowed and loses mass with increased atmospheric pressure and temperature (Melosh, 1981). Once the pressure on the meteor exceeds its strength,

fragmentation occurs, and a flash of light is observed; multiple stages of fragmentation can occur as pieces disperse from the main body. Fragments that retain enough inertial force to reach the surface can form craters, while fragments that do not retain enough inertial force enter "dark flight" (i.e. slowed to terminal velocity) as ablation ceases and do not form measurable craters. Just as scaling equations and models have been established to approximate the size of a crater formed by an impactor (Neukum et al., 2001), equations and models for the effect of an atmosphere on an incoming projectile's characteristics have also been developed.

Opik (1958) provides one of the first in-depth discussions on the physical phenomena of deceleration, mass loss, and fragmentation. He quantifies the transfer of energy between atmospheric molecules and the incoming meteor over time during flight, taking into account the atmospheric conditions at altitude, as well as the meteor's shape, rotation, composition, and compactness. Ablation occurs depending on the transfer of heat to the meteor and the heat of ablation with the conversion of solid material to vapor within the bow–shock formed around the incoming meteor. Öpik describes fragmentation as occurring when the stagnation point pressure at the front of the meteor (dependent on atmospheric density and velocity) exceeds the compressive or tensile strength of the material (depending on the shape of the object, categorized as spherical or non-spherical).

Baldwin and Sheaffer (1971) synthesized Öpik's theories along with other assumptions and observations into a model for the ablation and fragmentation of large meteoroids (>1,000 kg). Arc-jet wind tunnel experiments and strength measurements for carbonaceous chondrite, bronzite, and iron meteorites were used to establish ablation and fragmentation criteria. Consistent with Öpik's theory, the meteor breaks when the tensile and/or compressive strength is exceeded, and the number of fragments is dependent on the initial and current mass of the projectile at the time of fragmentation. In their study, fragmentation produces fragments that disperse laterally (pancake) in an increasing effective frontal area scaled appropriately to the total number of fragments. The altitude at which a projectile will fragment depends on its unique physical characteristics (composition, porosity, zones of weakness, compactness, shape) and its initial characteristics (mass, velocity, and angle of trajectory).

Researchers have explored different approaches over the decades to approximate fragmentation, such as mechanical methods that utilize predetermined thresholding or hydrodynamic methods that introduce projectile imperfections and account for random chance. Mechanical methodologies involve discretizing the physical effects on a single-bodied projectile, a concentration of fragments located behind a singular bow-shock, or as individual fragments with their own trajectories and bow-shocks (Passey & Melosh, 1980; Nicol et al., 1985; Chyba et al., 1993; Ceplecha & Revelle, 2005; Collins et al., 2005). 2D and 3D hydrodynamical models assume the impactor to be a strengthless fluid and use Eulerian (particle concentration) and free-Lagrangian (individual particle) theories of fluid flow, taking into account Rayleigh-Taylor (RT) and Kelvin Helmholtz (KH) instabilities (V. V. Shuvalov et al., 1999; Svetsov et al., 1995; Artemieva & Shuvalov, 2001; V. V. Shuvalov & Trubetskaya, 2010).

Expanding on terrestrial studies, atmospheric effects of other planetary bodies within our solar system have been modeled. For Mars's relatively thin atmosphere, investigations into the effects of the atmosphere on incoming projectiles have provided insights regarding spacecraft hazards during entry (Humes & Bess, 1972) and the possible depletion of its atmosphere with large impacts (Melosh & Vickery, 1989). For the gas giant Jupiter, observations of the Shoemaker-Levy 9 comet entering its atmosphere in 1994 have provided detailed insights into the catastrophic effect on an icy object into Jupiter's dense atmosphere (Mac Low & Zahnle, 1994; K. Zahnle & Mac Low, 1994). Theoretical models of the effects on comets traveling through the atmosphere of Titan, one of

Jupiter's satellites, predicts the smallest craters on that surface to be ∼2 km in diameter (Korycansky & Zahnle, 2005), similar to that of crater distributions seen on Venus.

The atmospheric effects of the Venusian atmosphere have attracted particular interest because of their extent relative to other terrestrial planetary bodies in the solar system. Schaber et al. (1992) suggest that the atmosphere potentially filters ∼98 % of projectiles that would form craters between 2 – 35 km in diameter in the absence of an atmosphere and that projectile mass is the dominant characteristic when determining the potential of forming a crater on the surface of Venus. Tauber and Kirk (1976) estimated the smallest craters on Venus to be on the order of 150 – 300 m. Thus, the loss of mass is a significant aspect of Venusian filtering; however, fragmentation appears to be the limiting factor on which projectiles can survive (Herrick & Phillips, 1994; Ivanov et al., 1992, 1997). Melosh (1981) observed that during fragmentation of projectiles for terrestrial craters > 1 km, the fragments tend to stay clustered together behind a single bow shock to produce a single crater, rather than dispersing into smaller units to produce a field of craters, and hypothesized that this threshold of craters produced in this single bow-shock manner, on Venus, must be > 10 km in diameter. Recent 2D and 3D hydrodynamic modeling of Venusian atmospheric effects (Korycansky et al., 2000, 2002; Korycansky & Zahnle, 2003, 2004, 2005) have constrained impactors to have initial masses $> 10^{12}$ kg yielding a surface age of 730 ± 110 Ma.

# 3 Methods

## 3.1 Overview

The Atmospheric Effects Model (AEM), presented here, tracks a user-defined projectile population through a target planet's atmosphere, numerically approximates atmospheric effects (mass loss, deceleration, trajectory, and fragmentation), and produces a corresponding population of impact craters for the projectiles that "survived" passage to strike the surface. Within AEM, a projectile is defined as a homogeneous sphere with physical characteristics (density, diameter, and mass) and initial travel characteristics (velocity and angle of trajectory). A planetary target is defined by its physical characteristics (radius, surface density, gravity, simple-to-complex crater diameter threshold, and crater modification threshold) and atmospheric conditions (scale height and vertical profiles in temperature, pressure, and density). Impact craters are produced as simple or complex, and AEM records the transient and final crater physical characteristics (diameter and depth).

The evolution of projectile characteristics during atmospheric flight are modeled using a series of sequential differential equations to approximate physical change over discrete time steps. The cumulative evolution of physical characteristics provides a discretized approximation of projectile evolution during atmospheric passage. Due to this iterative process, if a characteristic goes beyond its fundamental limit (e.g., mass decreases to < 0 kg or angle increases to > 90° relative to horizontal), the respective characteristic is artificially capped at its limit. If at any time step during descent to the surface, the projectile either 1) no longer has mass and/or 2) has reached terminal velocity, thus entering dark flight, calculations for that projectile cease, and it is presumed to no longer have enough inertial forces to form an impact crater. However, if a projectile "survives" descent to reach the surface, its final characteristics (mass, velocity, and angle) are used to calculate the crater characteristics dependent on the target planet characteristics. Figure 1 illustrates the atmospheric conditions (detailed in Section 3.2.1), projectile characteristics (detailed in Section 3.2.2), and atmospheric effects (detailed in Section 3.3), taken into account within AEM. This initial iteration of AEM provides an estimate of the minimum combination of projectile characteristics able to withstand atmospheric travel and the maximum potential crater size-frequency distribution.

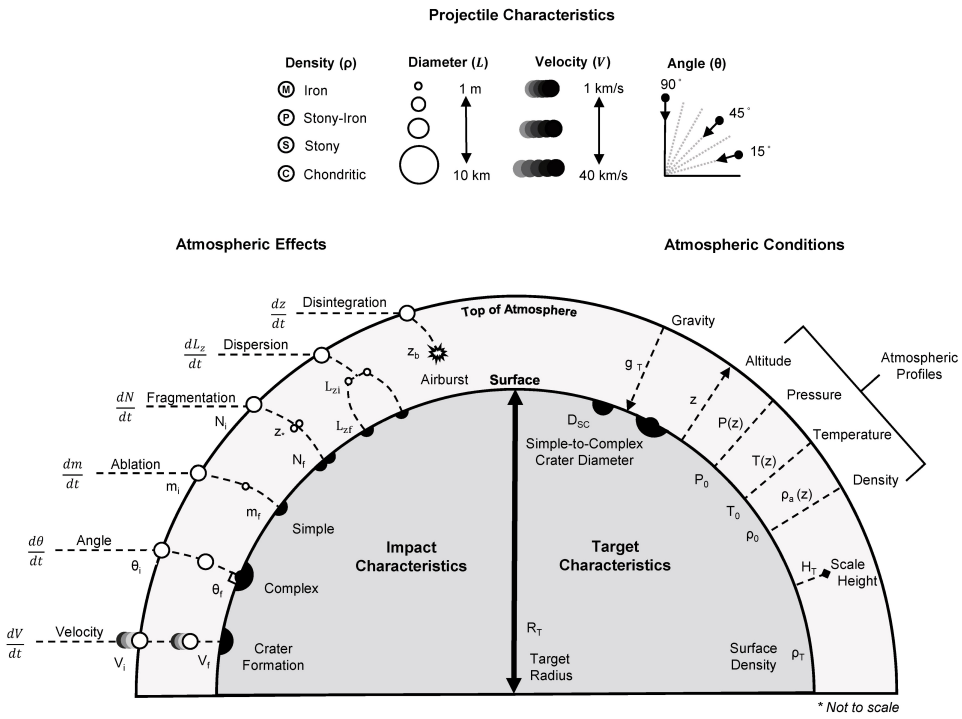


**Figure 1.** AEM diagram. A representation of all factors taken into account within AEM, including (top) characteristics of each projectile in the theoretical population evaluated in the study, (left) atmospheric effects and impact characteristics, and (right) atmospheric conditions and target characteristics. See Section 3.1 for reference.

With the inclusion of numerical atmospheric effect methodologies developed since the 1950s, AEM has been designed in a modular manner to allow for comparisons and sensitivity testing regarding choices of equations and assumptions used. This comparison of methods enables investigations into the spread of the resulting simulation ensembles for model and analytical error comparisons. AEM provides the choice of including any combination of atmospheric effects (deceleration, mass loss, and/or fragmentation) to allow testing of individual effects. The methodological equations used for atmospheric effects (deceleration, mass loss, etc.) are decided with a series of flag selections at the beginning of the MATLAB script, and certain assumptions regarding a projectile's interaction with the atmosphere (coefficients for lift $C_L$, drag $C_D$, heat transfer $C_H$, etc.) can either be set as a constant value throughout the model run or set to calculate at each time step (using a flagged equation). For transparency, the syntax of all equations and variables used in this study were homogenized from the original sources (e.g., standardizing variable symbols) to better facilitate comparison.

## 3.2 AEM Inputs

### *3.2.1 Target Characteristics*

Target planetary bodies used in this study (Venus, Earth, the Moon, and Mars) are modeled using a relatively simple set of characteristics and their current vertical atmospheric profiles for temperature, pressure, and density. In this study, all projectiles start at an initial altitude of 200 km above the surface, a conservative value that allows for easy/clean comparisons across different planetary bodies; however, the initial alti-

tude can be changed by the user to any given value or defined by the target's scale height ($H_T$) as the change in altitude over which the density and pressure decrease by 1/e. Profiles of temperature at discrete altitudes ($T_z$) for each target (Venus, Earth, and Mars) were referenced from Taylor et al. (2018), NOAA (1976), and Ramanan et al. (2013), respectively. Atmospheric temperature $T_z$ at one-meter altitude intervals were linearly interpolated from a discrete profile and calculated for each target by,

$$T_z = \frac{z - z_1}{\left(\frac{z_1 - z_0}{T_1 - T_0}\right)} + T_1 \tag{1}$$

where the altitude (z) and temperature ($T_z$) at a given point are calculated using the discrete altitudes ($z_1$, $z_0$) and temperatures ($T_1$, $T_0$) one-meter above and below the altitude in question respectively. Profiles of atmospheric pressure $P_z$ (Pa) and density $\rho_z$ (kg/m$^3$) at altitude for each target are defined by,

$$P_z = P_0 \times exp\left[\frac{-g_T M_n z}{R T_S}\right] \tag{2}$$

$$\rho_z = \rho_0 \times exp\left[\frac{-z}{H_T}\right] \tag{3}$$

where, $z$ is altitude, $P_0$, $\rho_0$, and $T_S$ are the atmospheric pressure, density, and temperature at the surface, $g_T$ is the target's gravity in $m/s^2$, $M_n$ is the mean atmospheric molecular weight (kg/mol), and $R$ is the universal gas constant (8.314 J/K/mol). See Figure 2 for atmospheric profiles of Venus, Earth, and Mars. During model runs, a projectile's altitude (z) is inputted to Equations 1, 2, and 3 to calculate atmospheric conditions at that time step.

Planetary target characteristics include the average distance from the Sun $X_T$ (m), orbital velocity $V_T$ (m/s), radius $R_T$ (m), surface density $\rho_T$ (kg/m$^3$), and the simple-to-complex crater threshold $D_{sc}$ (m) defined as the average inflection point between simple and complex crater diameters. To simulate the resistance of larger projectiles to modification during atmospheric flight, ablation and fragmentation apply to projectiles below a certain diameter $D_{mod}$ (m), which is dependent on the target's average inflection point for diameters of craters formed from dispersed fragments ($< D_{mod}$) and craters formed from fragments that impact as a single unit ($> D_{mod}$). $D_{mod}$ is ∼100 m for Mars (Toon et al., 1997), ∼1 km for Earth and ∼10 km for Venus (Melosh, 1981). See Table 1 for target characteristics.

#### *3.2.2 Projectile Population*

The projectile population matrix used as input for AEM is referred to as the "FLAVRS" matrix. The name and structure of FLAVRS are based on the initial projectile characteristics that the matrix defines: effective frontal cross-sectional area ($A$, m$^2$), diameter or "length" ($L$, m), angle of trajectory ($\theta$, deg.), velocity (V, m/s), density ($\rho$, kg/m$^3$), yield strength ($Y_i$, Pa), and mass ($M$, kg). FLAVRS matrices can be created using the FLAVRS Builder MATLAB script, which builds a population of projectiles with unique initial characteristics (velocity, angle, density, and diameter or mass) input by the user or a population using every combination of those characteristics. Sequential columns within FLAVRS matrix defines projectile characteristics while rows are individual projectiles (See Table 2 for reference).

Projectiles are assumed spherical by the rotational characteristics of a spinning object in flight through an atmosphere (Passey & Melosh, 1980); however, this may not be the proper assumption for studies of oblong/cylindrical projectiles. This iteration of AEM

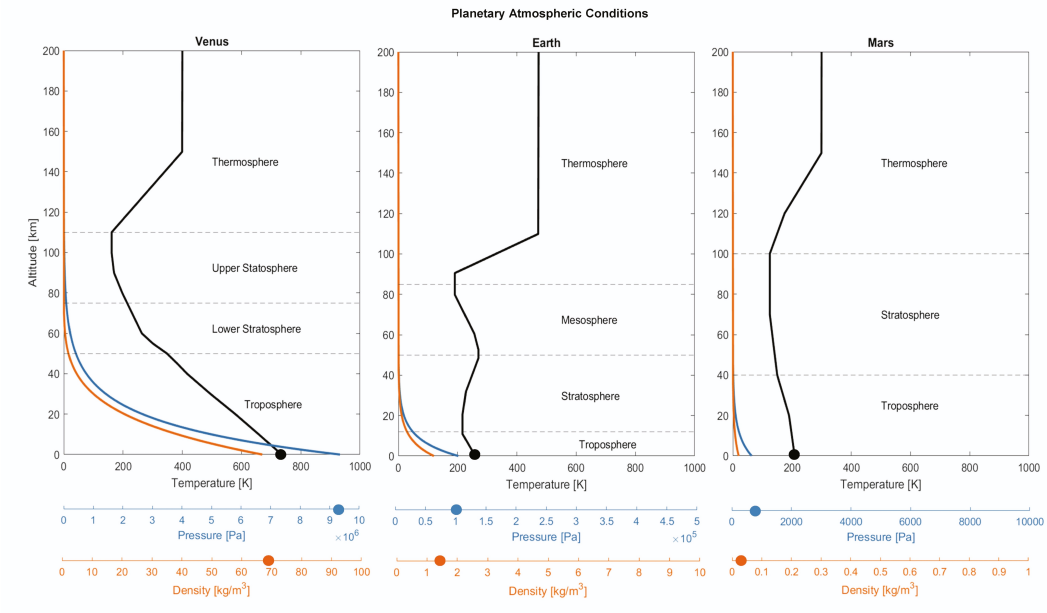


**Figure 2.** Modeled atmospheric profiles for Venus, Earth, and Mars. Atmospheric conditions of Venus (left), Earth (center), and Mars (right) at altitude, including temperature (black), pressure (blue), and density (orange) at altitude. Boundaries between distinct atmospheric zones are labeled and denoted with horizontal dashed lines. The surface temperature, pressure, and density for all three planets are marked on the x-axes. See Section 3.2.1 for reference.

**Table 1.** Planetary target characteristics. Characteristics for targets without a discernible atmosphere (i.e., the Moon) are omitted from the model. Characteristics from top to bottom: atmospheric temperature $T_S$ (K), density $\rho_0$ (kg), pressure $P_0$ (Pa) at the surface, and $M_n$ (kg/mol) mean molecular weight; planetary gravity $g_T$ (m/s$^2$), scale height $H_T$ (km), distance from the Sun $X_T$ (km), orbital velocity $V_T$ (km), radius $R_T$ (km); crater simple-to-complex threshold $D_{sc}$ (km) and modification threshold $D_{mod}$ (km). See Section 3.2.1 for reference.

| **Category** | **Characteristic** | **Venus** | **Earth** | **Moon** | **Mars** |
|---|---|---|---|---|---|
| Atmospheric | $T_S$ | 737 | 288 | - | 210 |
| | $\rho_0$ | 67.0 | 1.20 | - | 0.02 |
| | $P_0$ | $9.32 \times 10^6$ | $1.13 \times 10^5$ | - | 636 |
| | $M_n$ | 0.04334 | 0.02896 | - | 0.04334 |
| Planetary | $g_T$ | 8.87 | 9.81 | 1.62 | 3.71 |
| | $H_T$ | 15.9 | 8.5 | - | 11.1 |
| | $X_T$ | $1.082 \times 10^7$ | $1.496 \times 10^8$ | - | $2.279 \times 10^8$ |
| | $V_T$ | 35.02 | 29.78 | - | 24.07 |
| | $R_T$ | 6,052 | 6,378 | 1,738 | 3,396 |
| Crater | $D_{SC}$ | 40 | 3.20 | 15 | 9 |
| | $D_{mod}$ | 10 | 1 | - | 0.100 |

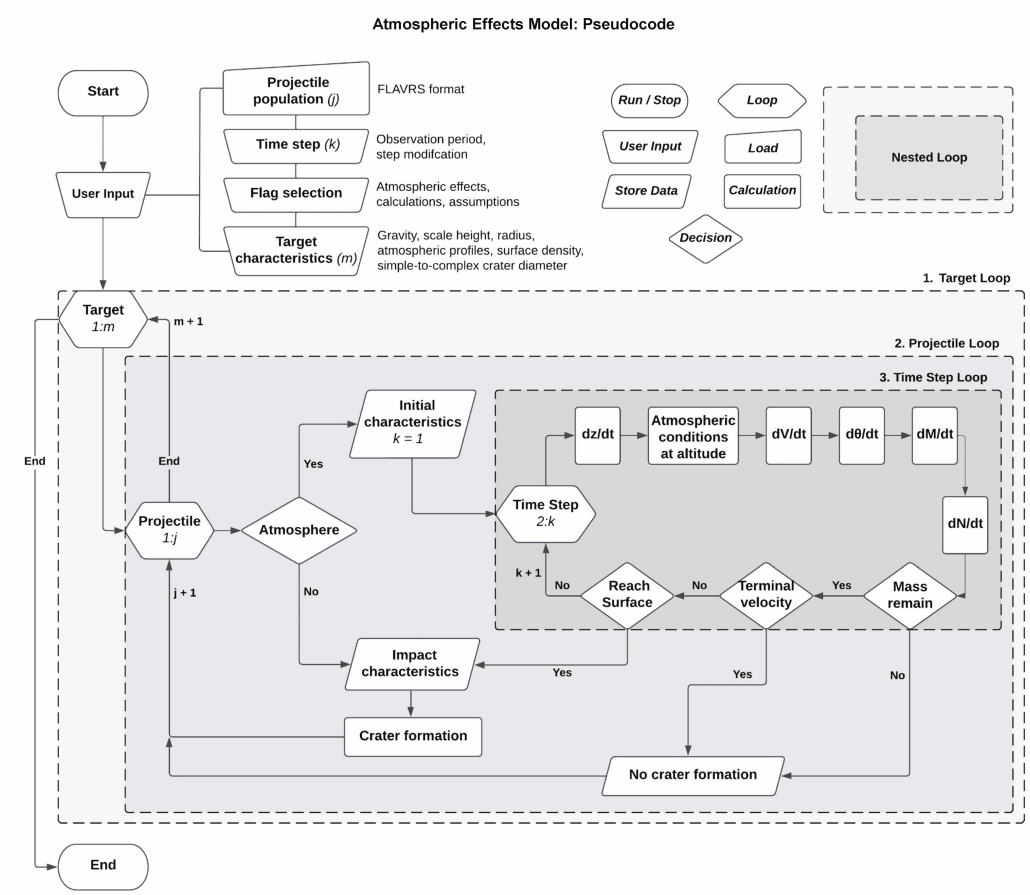


**Figure 3.** Flowchart of AEM pseudocode. Atmospheric Effects Model (AEM) script flowchart showing user inputs, the nested loop for calculating a projectile population to a target planetary body with or without an atmosphere, crater formation, and model outputs. See Sections 3.3 for reference.

includes calculations for spherical projectiles only. While porosity and zones of weakness introduce a level of unpredictability to a projectile's mass loss and fragmentation, we have assumed all projectiles to be rigid and homogeneous with no void space or weaknesses. This restriction to projectile characteristics was applied to investigate atmospheric effects under "ideal" conditions, keeping in mind that more realistic asteroids and meteoroids would ablate and fragment at a higher efficiency than AEM estimates.

### 3.3 Atmospheric Effects

Atmospheric effects are calculated using a nested loop, with the outermost loop processing each planetary target (1:m), m being the number of planetary targets, the middle loop processing each individual projectile (1:j), and the innermost loop processing each time step (1:k). These loops build a series of matrices tracking each parameter (altitude, velocity, etc.) for every projectile at each time step. The first column of each parameter's matrix holds the initial projectile characteristic, with each successive column in that row tracking the projectile's characteristics at each time step. For the evolution of each projectile characteristic, we have gathered equations and assumptions from the literature that simulate similar processes. We describe the sources of these equations further in this section, see Figure 3 for a reference flowchart of script processing.

For model runs, we define an observation period, along with a time step interval for incremental sampling, which in turn determines the resolution of discretized projectile evolution. For example, an observation period of 60 seconds, with a time step interval of 1 second, would calculate up to 60 discrete values during a projectile's descent to the target's surface. However, the greater the projectile's velocity, the fewer time steps it takes to reach the surface, assuming no atmospheric effects on deceleration or mass loss. To increase sampling resolution and better approximate changes between time steps, the time step can be modified by any increment of one second, as the projectile's velocity is given in m/s. If modified, the change in characteristics between time steps is divided by that modification value to approximate the effects over the incremented time interval. While a smaller time step interval provides higher sampling resolution, it also corresponds to longer processing times with diminishing returns on resolution at increments less than 1/10th of a second. With this trade-off between resolution and processing time, we chose 1/10th of a second as the optimal modification for balancing sampling resolution and processing time for both high and low–velocity projectiles.

The evolution of characteristics considered in AEM equations are calculated in sequential time-step order, with calculations using a characteristic from the current and/or previous time step. As the difference in time step characteristics is minimal between modified time steps, a tenth of a second in this case, this assumption was shown to not significantly affect the overall approximation of projectile evolution. Note that the equations described in this section define the change over one unmodified time step, which is then incrementally sampled by the time step modification.

#### *3.3.1 Change in Altitude*

The numerical approximation of the change in altitude for an incoming projectile is consistently defined throughout the literature (Artemieva & Shuvalov, 1996; Baldwin & Sheaffer, 1971; McAuliffe & Christou, 2006; Nicol et al., 1985; Passey & Melosh, 1980) by,

$$\frac{dz}{dt} = -V \sin\theta \tag{4}$$

where z is altitude (km), t is time (s), V is the velocity (km/s), and $\theta$ is the angle of trajectory relative to horizontal.

#### *3.3.2 Change in Velocity*

Since velocity has a greater effect on the change in altitude than the angle of trajectory (sin$\theta$ being between 0 and 1), it is the next calculated effect after change in altitude. In the AEM MATLAB script, specific calculations and assumptions are called with flag selections by the year of publication. For example, using the change in velocity equation from Baldwin and Sheaffer (1971) would be input as flag.vel = [1971], and if two were published in the same year then identifiers can are added as flag.vel = [1971.1]. The change in velocity can be calculated by,

Opik (1958)

$$\frac{dV}{dt} = -\frac{C_D \rho_z S_F V^2}{M^{1/3} {\rho_m}^{2/3}} \tag{5}$$

Baldwin and Sheaffer (1971)

$$\frac{dV}{dt} = -\frac{1}{2} C_D \rho_z V^2 \frac{A}{M} + g_T \cos\theta_v \tag{6}$$

Passey and Melosh (1980)

$$\frac{dV}{dt} = -\frac{C_D \rho_z A V^2}{M} + g_T \sin\theta \tag{7}$$

Chyba et al. (1993)

$$\frac{dV}{dt} = \frac{-\frac{1}{2} C_D \rho_z A V^2 + \frac{g_T}{M} \sin\theta}{M} \tag{8}$$

Svetsov et al. (1995)

$$\frac{dV}{dt} = \frac{-\frac{1}{2} C_D \rho_z A V^2}{M} \tag{9}$$

Artemieva and Shuvalov (1996)

$$\frac{dV}{dt} = -C_D \frac{\rho_z A V^2}{2M} \tag{10}$$

Korycansky and Zahnle (2003)

$$\frac{dV}{dt} = \frac{-C_D \rho_z A V^2}{M} \tag{11}$$

Campbell-Brown and Koschny (2004)

$$\frac{dV}{dt} = -\frac{C_D \rho_z V^2}{M} A \left[\frac{M}{\rho_m}\right]^{2/3} \tag{12}$$

Collins et al. (2005)

$$\frac{dV}{dt} = -\frac{3 C_D \rho_z}{4 \rho_m L} V^2 \tag{13}$$

where, $C_D$ is drag coefficient, $S_F$ is projectile shape factor, M is mass ($kg$), $\rho_m$ is projectile density (kg/m$^3$), L is diameter, the angle of trajectory relative to vertical is $\theta_v$ and horizontal is $\theta$. The effective cross-sectional area A ($m^2$), (Baldwin & Sheaffer, 1971; Passey & Melosh, 1980) is defined as:

$$A = S_F N^{1/3} \left[\frac{M}{\rho_m}\right]^{2/3} \tag{14}$$

The number of fragments N remains constant at 1 when no fragmentation or dispersion has occurred.

When assuming a constant projectile shape, the shape factor $S_F$ for a sphere has been agreed upon in the literature to be either 1.21 (Humes & Bess, 1972; Passey & Melosh, 1980; Nicol et al., 1985; Flynn et al., 2018) or calculated by,

(Assumed constant)

$$S_F = 1.21$$

Svetsov et al. (1995)

$$S_F = \pi {R_m}^2 M^{-2/3} {\rho_m}^{2/3} \tag{15}$$

where, $R_m$ is the radius of the projectile.

As AEM calculates the mass and radius of a projectile assuming a spherical shape, the drag coefficient $C_D$ is assumed to be 0.47 for a rigid sphere (Hoerner, 1965). However, $C_D$ for a sphere can be calculated using the circular frontal area $A_C$ or with the Reynolds number $Re$ of the projectile through the atmosphere by,

(Assumed constant)

$$C_D = 0.47$$

Baldwin and Sheaffer (1971)

$$C_D = 1 + e^{(-1.837\times10^6)\frac{\rho_z}{\rho_0}A_c} \tag{16}$$

Khanukaeva (2003)

$$C_D = 1 + e^{-Re} \tag{17}$$

Morrison (2013)

$$C_D = \frac{24}{Re} + \frac{2.6(\frac{Re}{0.5})}{1+(\frac{Re}{5.0})^{1.52}} + \frac{0.411(\frac{Re}{2.63\times10^5})^{-7.94}}{1+(\frac{Re}{2.63\times10^5})^{-8.00}} + \frac{0.25(\frac{Re}{10^6})}{1+(\frac{Re}{10^6})} \tag{18}$$

where $A_C$ is the circular frontal area (Baldwin & Sheaffer, 1971), and the Reynolds number $Re$ is the ratio between the inertial forces of the projectile and the viscous forces of the atmosphere (Morrison, 2013), is calculated by,

$$A_C = \pi^{-1/2} S_F^{1/2} \rho_z^{-1/3} M^{1/3} N^{-1/3} \tag{19}$$

and the Reynolds number $Re$ is the ratio between the inertial forces of the projectile and the viscous forces of the atmosphere (Morrison, 2013), is calculated by,

$$Re = \frac{\rho_a V L}{\mu} \tag{20}$$

where $\mu$ is the dynamic viscosity (Ns/m$^2$) of air dependent on temperature. When the Reynolds number is higher, the flow behind the projectile becomes more turbulent and drag increases (Khanukaeva, 2003; Naganna et al., 2017; Moilanen et al., 2021).

#### *3.3.3 Change in Angle*

A projectile's angle of trajectory relates to the amount of atmosphere it encounters during flight. The more oblique the angle ($< 45°$ relative to horizontal), the greater amount of atmosphere the projectile encounters before reaching the surface. The change in angle can be calculated by,

Baldwin and Sheaffer (1971)

$$\frac{d\cos\theta_v}{dt} = \frac{g_T}{V}\left(1-\cos^2\theta_v\right) \tag{21}$$

Passey and Melosh (1980)

$$\frac{d\theta}{dt} = \frac{Mg_T\cos\theta - \frac{C_L\rho_z A V^2}{2}}{MV} - \frac{V cos\theta}{R_T + z} \tag{22}$$

Chyba et al. (1993)

$$\frac{d\theta}{dt} = \frac{g_T\cos\theta}{V} - \frac{C_L\rho_z A V}{2M} - \frac{V cos\theta}{R_T + z} \tag{23}$$

Artemieva and Shuvalov (1996)

$$\frac{d\theta}{dt} = \frac{2Mg_T\cos\theta - C_L\rho_z A V^2}{2MV} \tag{24}$$

The lift coefficient $C_L$ is generally assumed constant between 0 – 0.01, but can be as high as 2 depending on the mass, angle of trajectory, and dispersion of fragments (Passey & Melosh, 1980; Artemieva & Shuvalov, 1996; Aziz et al., 2008). Passey and Melosh (1980) suggested that the lift coefficient of an incoming projectile is relatively insignificant and varies between a value of 0 and 0.01 but should be a maximum of 0.01 for masses between $10^7$ – $10^8$ kg and angles between 15° - 45° with respect to horizontal. In this study, we assume lift to remain constant at 0.01 (Passey & Melosh, 1980), as the maximum amount of lift required to produce a strewn field with the largest crater at the downrange, but it could be calculated by,

(Assumed constant)

$$C_L = 0.01$$

Passey and Melosh (1980)

$$C_L = 2Mg_T \cos\theta / \rho_z A V^2 \tag{25}$$

#### *3.3.4 Change in Mass*

Equations for mass evolution have remained relatively consistent throughout the literature. However, the assumptions made in mass loss calculations, such as drag coefficient ($C_D$), lift coefficient ($C_L$), and others, can greatly influence the approximated trajectory of the projectile. With our assumption of mass loss not affecting projectiles over a certain diameter $D_{mod}$ (100 m for Mars (Toon et al., 1997), 1 km for Earth and 10 km for Venus (Melosh, 1981)), ablation effects are calculated if a projectile begins with a diameter less than this threshold; otherwise mass remains unchanged. The change in a projectile's mass over time can be calculated by,

Opik (1958)

$$\frac{dM}{dt} = -\frac{C_H \rho_z S_F V^3 M^{2/3}}{2\zeta {\rho_m}^{2/3}} \tag{26}$$

Baldwin and Sheaffer (1971)

$$\frac{dM}{dt} = -\frac{1}{2} C_H \rho_z V^3 \frac{A}{\zeta} \tag{27}$$

Passey and Melosh (1980)

$$\frac{dM}{dt} = -\frac{1}{2}\frac{C_H \rho_z A V^3}{\zeta}\left(\frac{V^2 - {V_{CR}}^2}{V^2}\right) \tag{28}$$

Bronshten (1983)

$$\frac{dM}{dt} = -C_H \frac{\rho_z A V^3}{2\zeta} \tag{29}$$

Chyba et al. (1993)

$$\frac{dM}{dt} = \frac{-\frac{1}{2} C_H \rho_z A V^3}{\zeta} \tag{30}$$

Campbell-Brown and Koschny (2004)

$$\frac{dM}{dt} = -\frac{C_H A}{2L}\left(\frac{M}{\rho_m}\right)^{2/3} \rho_z V^3 \tag{31}$$

where, according to Passey and Melosh (1980), $V_{CR}$ is the critical velocity (3 km/s) below which steel pellets experimentally do not glow at sea level, $C_H$ is the heat transfer coefficient which can range between 0.01 – 6.0 and generally assumed to be 0.02, and

the heat of ablation ($\zeta$) can be assumed $5.0\times10^6$ J/kg between the heat of fusion ($1.89\times 10^6$) and vaporization ($8.01 \times 10^6$) of an iron meteorite.

If, at any time step, the projectile no longer has any mass remaining and/or has reached terminal velocity, calculated by,

$$V_t = \sqrt{\frac{2Mg_T}{C_D\rho_z A_c}} \tag{32}$$

The projectile is then assumed to no longer have sufficient inertial energy to form a noticeable impact crater on the target surface. When this occurs, the nested loop breaks out of the innermost time-step loop and calculations for that projectile cease. However, if the projectile reaches the target surface (z = 0) with mass remaining and above the terminal velocity, the final projectile characteristics are stored to approximate the size and depth of the crater to be formed.

#### *3.3.5 Fragmentation*

The modularity of AEM allows comparison and testing of many atmospheric effect methodologies. This modularity includes how we simulate when, where, and how a projectile will break into fragments. In this study, we integrated the methodologies of Baldwin and Sheaffer (1971); Passey and Melosh (1980) and Collins et al. (2005) with our discretized observation intervals to approximate the number of fragments a projectile breaks into and how far they disperse, or "pancake," away from the main body. With our assumption of fragmentation not affecting projectiles over a certain diameter ($D_{mod}$), fragmentation effects are calculated if a projectile begins with a diameter less than this threshold; otherwise, the number of fragments remains unchanged at one. Fragmentation occurs when the stagnation pressure $P_s$ (Passey & Melosh, 1980) on the face of the projectile exceeds its yield strength $Y_i$ (Collins et al., 2005), calculated by,

$$P_s = \rho_z V^2 \tag{33}$$

$$Y_i = 10^{2.107+0.0624\sqrt{\rho_m}} \tag{34}$$

where, the yield strength is defined as the empirical relationship between the strength and density of the projectile's composition (chondritic, stony, stony-iron, or iron). At the time step when the strength threshold is exceeded, the projectile breaks into one additional fragment (N+1) being one-half the mass of the next largest fragment (Baldwin & Sheaffer, 1971). According to Collins et al. (2005), as the fragments disperse laterally the pancaked diameter $L_p$ is calculated as,

$$L_p = L\sqrt{1 + \left(\frac{2H}{l}\right)^2 \left(exp\left[\frac{z^* - z}{2H}\right] - 1\right)} \tag{35}$$

$$l = L\sin\theta\sqrt{\frac{\rho_m}{C_D\rho_z}} \tag{36}$$

where, L and $L_p$ are the projectile diameter beforehand and after pancaking, and $z^*$ and $z$ are the altitude at which it fragments and the altitude at each time step respectively. The pancaked effective area is then calculated using Equation (14). The pancake factor $f_p = L_p/L_0$ approximates the total dispersion of fragments (where$L_0$ is this initial diameter) and once exceeded, results in an airburst. The projectile is then assumed

to no longer have sufficient inertial force remaining to form a crater. The pancake factor at airburst has been approximated between 2 – 4 (Ivanov et al., 1997), 5 – 10 for Tunguska-like events (Chyba et al., 1993) and 7 (Collins et al., 2005). Based on our preliminary experimentation for a Tunguska-like impactor, we have chosen a limit of 5. However, this value can be defined by the user.

### 3.4 Crater Formation

At the time step a projectile reaches an altitude of 0 km, the final projectile characteristics (diameter, mass, velocity, angle) are used to derive the relative crater size using standard scaling equations. The transient crater diameter $D_{tc}$ (m) and depth $d_{tc}$ (m) (Collins et al., 2005) are calculated by,

$$D_{tc} \approx 1.161 \left(\frac{\rho_m}{\rho_t}\right)^{1/3} {L_f}^{0.78} {V_f}^{0.44} {g_T}^{-0.22} \sin^{1/3}\theta_f \tag{37}$$

$$d_{tc} \approx \frac{D_{tc}}{2\sqrt{2}} \tag{38}$$

where, $\rho_t$ is the density of the target surface (kg/m$^3$). In this study, for simplicity and ease of comparison between targets, all targets are assumed to have the average surface density of rocks found in Earth's crust ∼2,830 kg m$^3$ (Christensen & Mooney, 1995). However, surface densities can be defined for each target by the user. The final crater diameter is determined by the target's simple-to-complex crater diameter threshold $D_{sc}$, where over a certain diameter the majority of craters are classified as complex and have either a central peak or ring.

If the transient diameter is less than the $D_{sc}$ threshold, a simple crater diameter $D_{fr}$ and depth $d_{fr}$ are calculated by,

$$D_{fr} \approx 1.25 D_{tc} \tag{39}$$

$$d_{fr} = d_{tc} + h_{fr} - t_{br} \tag{40}$$

$$h_{fr} = 0.07 \frac{{D_{tc}}^4}{{D_{fr}}^3} \tag{41}$$

$$t_{br} \approx 2.8 V_{br} \left(\frac{d_{dt} + h_{fr}}{d_{tc} {D_{fr}}^2}\right) \tag{42}$$

$$V_{br} \approx 0.032 {D_{fr}}^3 \tag{43}$$

where, the brecciated lens that fills a portion of the final crater's depth is measured using $h_{fr}$ (thickness of the ejecta), $t_{br}$ (thickness lens itself), and $V_{br}$ (the volume of the lens).

If the transient diameter is greater than the $D_{sc}$ threshold, a complex crater diameter $D_{fc}$ and depth $d_{fc}$ are calculated by:

$$D_{fc} = 1.17 \frac{{D_t}^{1.13}}{{D_{sc}}^{0.13}} \tag{44}$$

$$d_{fc} = 1.04{D_{fc}}^{0.301} \tag{45}$$

Note that scaling constants are generally ill-constrained and can vary within a few decimal places (Collins et al., 2005); for example, the constant 1.17 (e.g., Equation 44) can vary between 0.8 – 1.5. Standard scaling constants for single terrestrial (Earth) craters were used across all planetary targets for comparison.

### 3.5 AEM Outputs

AEM records projectile characteristics and atmospheric conditions at each time step during a projectile's descent to a target's surface. We simulated atmospheric effects for all projectiles, terrestrial and theoretical, in AEM impacting the Lunar surface (representing no atmospheric effect) and evolve through the current atmospheric profiles of Mars (representing the lesser effect end member), Earth (representing the ground truth), and Venus (representing the greater effect end member). Projectile outputs include altitude ($z$), angle ($\theta$), effective circular frontal area ($A_C$), diameter ($L$), drag coefficient ($C_D$), number of fragments ($N$), pancake factor ($f_p$), heat of ablation ($\zeta$), lift coefficient ($C_L$), mass ($M$), percent of mass remaining, Reynold's number if used ($Re$), shape factor ($S_F$), velocity ($V$), velocity at fragmentation ($V^*$), altitude of fragmentation ($z_*$), altitude of airburst ($z_b$). Atmospheric conditions include pressure ($P_z$), temperature ($T_z$), and density ($\rho_z$) at each time step. If a crater is formed, the transient diameter ($D_t$) and depth ($d_t$), simple or complex classification, final diameter ($D_f$) and depth ($d_f$) are also recorded. Thus, AEM produces an in–depth approximation of a projectile's evolution and the resulting crater characteristics.

### 3.6 Experimental Procedures

#### *3.6.1 Model Sensitivity to Equations and Assumptions*

Given the modularity of AEM, with various equations and assumptions to choose from, a set of parameters and equations must be selected prior to running the model. While the numerical model itself does not introduce error per se, the assumptions within the model introduce de facto biases. To constrain the magnitude of this error, we tested the outputs from various sets of parameters and compared the spread of the ensemble and thus the sensitivity of the model to these parameters. Model equations to choose from include those detailed in Section 3.3, including the change in velocity ($dV/dt$), angle of trajectory ($d\theta/dt$), and mass ($dM/dt$); while assumptions to choose from are the shape factor ($S_F$), drag coefficient ($C_D$), lift coefficient ($C_L$), heat transfer coefficient ($C_H$), and the heat of ablation ($\zeta$).

To model sensitivity, a Meteor Crater-like impactor (iron, 50 m, 17 km/s, 45°) entering Earth's atmosphere was simulated with varying sets of model equations and parameters. We tested a range of equation and assumption by varying it while all other model parameters were held constant. We used the following as our baselines: equations for the change in velocity, mass, and angle were calculated using Baldwin and Sheaffer (1971) Equations 6, 21, and 27 and assumptions: $(S_F) = 1.21$, $(C_D) = 0.47$, $(C_L) = 0.01$, $(C_H) = 0.02$, and $\zeta = 5{\times}10^6$, referenced from previous studies on terrestrial (Earth) atmospheric filtering (Baldwin & Sheaffer, 1971; Passey & Melosh, 1980; Collins et al., 2005). We also examined the sensitivity of crater formation with the total atmospheric effect (deceleration, mass loss, and fragmentation) on projectiles across all planetary targets. It should be noted that results would be different if different parameters were chosen; however, the conclusions of these experiments are consistent across varying parameters, and the comparison here is intended to determine how our methodologies and assumptions affect model output results.

**Table 2.** Terrestrial analog projectile population. FLAVRS matrix for initial characteristics of hypothesized projectiles for the formation of Chicxulub Crater, Meteor Crater, the Tunguska airburst, and the Chelyabinsk meteor. From left to right, cross-sectional area A ($m/s^2$, diameter L (m), angle $\theta$ (deg.), velocity V (km/s), density $\rho$ ($kg/m^3$), yield strength $Y_i$ (Pa), and mass M (kg). See Section 3.6.2 for reference.

| **Feature** | $A^*$ $m^2$ | $L$ $m$ | $\theta$ $deg.$ | $V$ $km/s$ | $\rho$ $kg/m^3$ | $Y_i{}^*$ $Pa$ | $M^*$ $kg$ |
|---|---|---|---|---|---|---|---|
| Chicxulub | $1.54 \times 10^8$ | 14,000 | 45 | 17 | 2,700 | $2.24 \times 10^5$ | $3.88 \times 10^{15}$ |
| Meteor | 1,965 | 50 | 45 | 17 | 7,800 | $4.15 \times 10^5$ | $5.11 \times 10^8$ |
| Tunguska | 1,965 | 50 | 45 | 17 | 2,700 | $2.24 \times 10^5$ | $1.77 \times 10^8$ |
| Chelyabinsk | 314 | 20 | 20 | 17 | 3,300 | $4.92 \times 10^5$ | $1.38 \times 10^7$ |

*Calculated within script using initial characteristics, others are given.

#### *3.6.2 Model Optimization using Terrestrial Analogs*

To test the validity of AEM approximations of planetary atmospheric effects, we tested AEM through Earth's atmosphere to compare it with (direct and indirect) observationally constrained impact and meteoric events. We maintained consistent equation and assumption flags throughout experimentation as outlined in Section 3.6. The observation period was 70 seconds with a time step increment of 1/10th of a second. Each run also simulated a projectile population's evolution through each of the planetary target atmospheres of Venus, Earth, and Mars. To assess the model's robustness to variances in projectile behavior, two runs were approximated for each: one with ablation (mass loss) only and another with ablation and fragmentation. See Table 2 for the terrestrial analog FLAVRS matrix (n = 4).

Notable terrestrial craters include Chicxulub and Meteor Crater. Chicxulub Crater (180 km in diameter) was likely formed by a chondritic asteroid impacting the Yucatan Peninsula in modern-day Mexico at 17 km/s at 45° (∼65 million years ago) (Collins et al., 2005). Meteor Crater (1.18 km) was likely formed by an iron asteroid Canyon Diablo meteor impacting Arizona, USA at an estimated between 12-17 km/s at 45° (> 50,000 years ago). While the theorized final Meteor Crater impact velocity varies slightly across studies (Melosh & Collins, 2005; Artemieva & Pierazzo, 2009), the Chixculub impactor has been estimated to have a diameter anywhere between 10 and 81 km (Durand-Manterola & Cordero-Tercero, 2014); however, crater scaling laws suggest a likely diameter of ∼14 km (Collins et al., 2005), while the denser Canyon Diablo meteor could have had a diameter of ∼50 m (Artemieva & Pierazzo, 2009). Furthermore, as no observations were recorded of these impacts, projectile diameters are ill-constrained and generally based on the most likely characteristics given the average asteroid impact angle (45°) and velocity (17 km/s) to Earth.

Notable meteor phenomena on Earth include the Tunguska airburst and the Chelyabinsk bolide. The Tunguska airburst flattened ∼2,150 $km^2$ of Russian forest in 1908 when an ∼50 m, potentially chondritic, meteor exploded at altitude (10 km) with the force of 15 megatons (Chyba et al., 1993; Turchak & Gritsevich, 2014). The Chelyabinsk meteor sightings in Russia (2013) were of an ∼20 m stony meteor producing a sonic boom and impacting at an oblique angle of 20°, with the largest fragment forming an ∼8 m wide hole in a frozen lake (Borovicka et al., 2013; Popova et al., 2013; Trigo-Rodríguez et al., 2021).

**Table 3.** Theoretical projectile population. Initial FLAVRS characteristics input to develop the theoretical population, angles of trajectory are relative to horizontal. Each combination of characteristics was used for a total of 4,992 projectiles. See Section 3.6.3 for reference.

| Characteristic | Inputs | Total |
|---|---|---|
| Diameter (km) | 1, 10, 15, 20, 25, 30, 35, 40, 45, 50, 60, 75, 100, 150, 200, 250, 350, 500, 750, 1000, 1500, 2500, 3500, 5000, 7500, 10000 | 26 |
| Density (kg/m$^3$) | 2700, 3300, 4500, 7800 | 4 |
| Velocity (km/s) | 1, 5, 10, 15, 20, 25, 30, 40 | 8 |
| Angle (deg) | 15, 30, 45, 60, 75, 90 | 6 |
| Total | | 4,992 |

#### *3.6.3 Theoretical Projectile Population*

To test the survivability of projectiles through the atmospheres of Venus, Earth, and Mars, we developed a theoretical population of projectiles for the inner solar system based on the range of observed asteroid and meteoroid characteristics. Observed projectiles can range in diameter from meteoroids [1 m – 1 km) to asteroids (>1 km], and have variable density (chondritic, stony, stony–iron, and iron). On average, observed projectile velocities can range anywhere from 10-20 km/s (asteroids and meteoroids) and up to 72 km/s (long-period comets) (Toon et al., 1997). The average non-cometary impact velocity is 9.4 km/s for Mars, 19.3 km/s for Earth, and 24.2 km/s for Venus (Ivanov, 2008). The average trajectory angle is normally distributed around 45° (Hughes, 1993). From these observations, initial characteristics for the theoretical projectile population span diameters (1 m – 10 km), densities (chondritic, stony, stony-iron, and iron), and thus masses ($1.41\times10^3$ - $4.08\times10^{15}$ kg), angles of trajectory (15 – 90°), and velocities (1 – 40 km/s). Using the characteristics outlined in Table 3 below, with a total of 4,992 projectiles, this population covers the gamut of masses and velocities likely to enter a planet's atmosphere and can provide estimates on the limitation of projectile survivability to each target.

## 4 Results

### 4.1 Model Sensitivity to Equations and Assumptions

When testing the sensitivity of AEM to variations in methodological equations and/or unconstrained assumptions, we held all other parameters constant. Projectile deceleration and mass loss for each of the equation options for velocity, mass, and angle of trajectory are shown in Figure 4, while variances in parameter assumptions on model results are shown in Figure 5. Varying equations and assumptions often provided results within reasonable agreement with the literature; however, some substantial differences were found for certain equation and parameter choices.

For a Meteor Crater-like impactor, as described in Section 4.1, eight of the nine velocity equations investigated in this study output similar impact velocities (7 – 13 km/s) and remaining masses (48 – 64%). Velocity Equation 13 (Collins et al., 2005) produced a projectile evolution that slowed drastically between the altitudes of 40 – 90 km, consistent with observed altitudes of deceleration and mass loss. All four angle equations output similar results (11 km/s impact, with ∼50% mass remaining) with no significant difference in deceleration or mass loss. Four of the six mass equations output similar results for deceleration (11 – 13 km/s) and mass loss (∼50%); however, Equation 26 (Opik, 1958) and Equation 29 (Bronshten, 1983) reduced mass by 20% and 60% respectively, with mass being lost substantially above 50 km altitude using Equation 29.

For a rigid sphere, such as the one modeled here, the shape factor is assumed to be 1.21 (Humes & Bess, 1972; Passey & Melosh, 1980; Nicol et al., 1985; Flynn et al., 2018) with a drag coefficient of 0.47 by default (Hoerner, 1965). However, to test the sensitivity of final calculations to variations (if assumed incorrectly) in shape factor and drag coefficient, we tested a range of values for each. The shape factor when assumed constant as 1.21 (sphere), 1.919 (hemisphere), or 4.28 (tube-like cylinder), yielded impact velocities between 4 – 11 km/s and remaining masses between 35 – 55%. Drag coefficients calculated using a constant of 0.47 or calculated using Equations 15 (Svetsov et al., 1995) and Equation 17 (Khanukaeva, 2003) yielded similar results of 11 km/s at 55% mass remaining. Higher drag coefficients of 1 and 2 or calculated using Equation 16 (Baldwin & Sheaffer, 1971), yielded slower impact velocities between 4 - 7 km/s and lower mass loss, retaining 66 – 78%. Lift coefficients between 0 – 2 and calculated using Equation (24) (Artemieva & Shuvalov, 1996) produced similar results of an impact at ∼11 km/s with 55% mass remaining.

The heat transfer coefficient and the heat of ablation had the most significant influence on impact characteristics. The heat transfer coefficient (when assumed between 0.01 – 0.02) produced the same impact velocity (∼11 km/s) but mass losses of 25 – 45% respectively. A heat transfer coefficient of 0.1 slowed the projectile to 7 km/s and ablated nearly all of its mass below an altitude of 40 km (reaching a pancake limit of 3); however, a coefficient of 0.6 vaporized the projectile completely above 17 km. The heat of ablation (J/kg ) for an iron meteorite can range between its heat of fusion ($1.89\times10^6$ J/kg ) to its heat of vaporization ($8.01\times10^6$ J/kg ); these end-members of ablation produced velocities within 1 km/s of each other (11 – 10 km/s respectively) and remaining masses between 15 – 75% respectively. All tested variations in equations and parameters resulted in only small variations in angle, as impact angles were generally within ∼0.02° of each other.

### 4.2 Terrestrial Analogs on Earth

We applied AEM to the four terrestrial examples described in Section 3.6.2 and Table 2, using AEM's approximation of Earth's current atmosphere. Model projectile evolutions for velocity and remaining mass and impact characteristics suggest that the model broadly performed as anticipated. Initial vs final projectile characteristics, transient and final crater diameters and depths, along with the maximum pancake factor and altitude of possible airburst were produced within reasonable ranges, though some differences with observes or estimate trajectories and craters persisted. See Figures 6 and 7 for reference.

The modeled Chicxulub impact characteristics were similar across both ablation only and ablation with fragmentation runs. The projectile decreased in mass by less than 1%, and in velocity by $< 0.5$ km/s for both runs. The impact produced a simulated Chicxulub Crater with a diameter of ∼135 km, compared to the actual ∼180 km in diameter, and a final depth of ∼4.5 km for both runs, compared to the actual which fluctuates from the crater rim, central ring, and crater center between ∼1 – 5 km. Results suggest that the Chicxulub projectile likely did not fragment and did not pancake during atmospheric travel.

The modeled Meteor Crater mass decreased by ∼51 – 77% and slowed to ∼11 and 15 km/s, for runs with ablation and fragmentation or ablation only respectively. This range encompasses prior simulations of impact velocity (Melosh & Collins, 2005; Artemieva & Pierazzo, 2009). The impact produced a simulated Meteor Crater with a diameter between ∼1.18 – 1.48 km compared to the actual 1.18 km diameter, and a final depth of ∼256 – 321 m compared to the actual 170 m. The modeled Meteor Crater projectile began to fragment at an altitude of 36 km and dispersed to a maximum pancake factor of 3.11 at an altitude of 11.2 km.

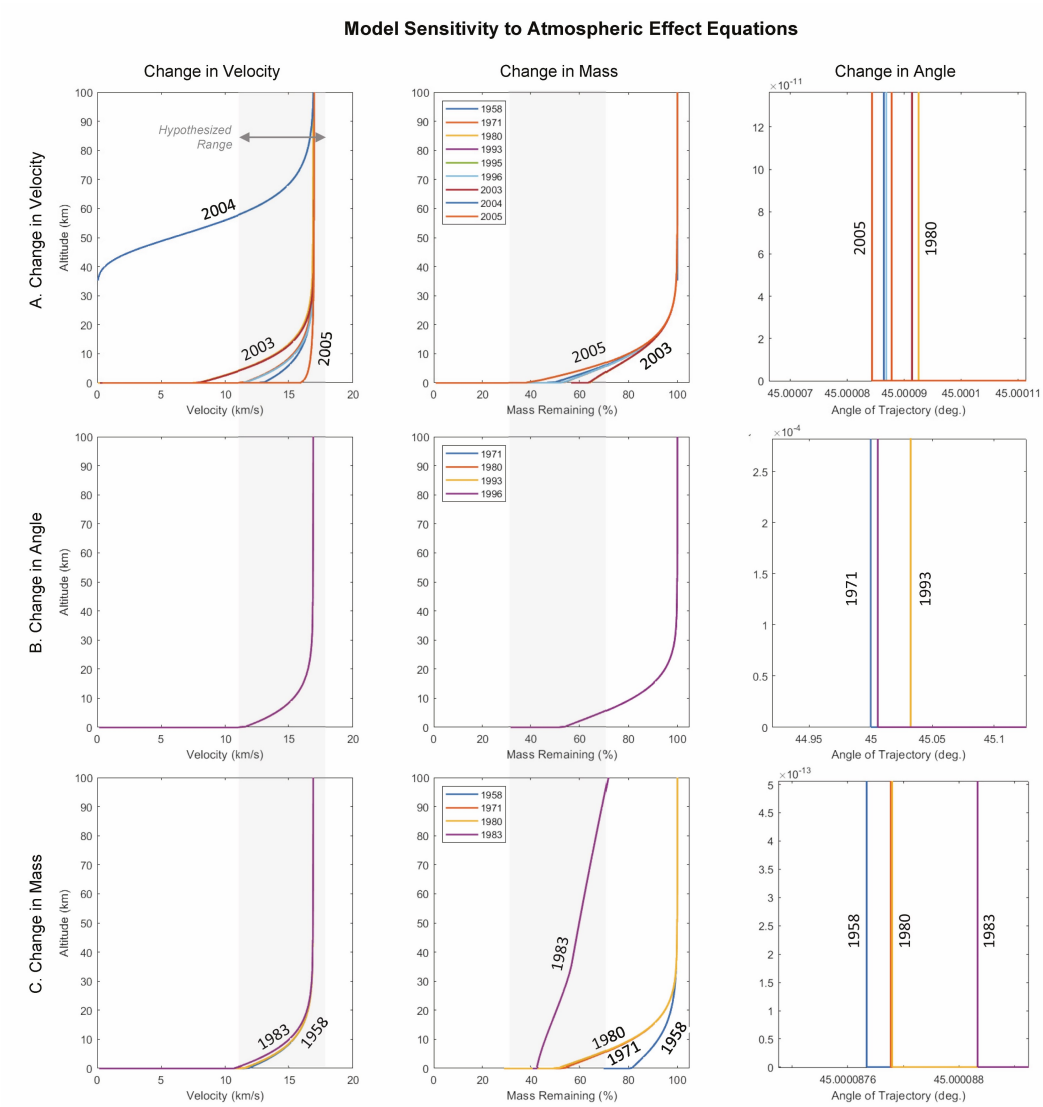


**Figure 4.** Sensitivity tests of velocity, mass, and angle equations. Model results using the varying equations for a projectile's change in velocity (A), angle of trajectory (B), and mass (C); while all initial characteristics for a Meteor Crater-like projectile (50m in diameter, iron density (7,800 kg/m$^3$), 17 km/s, at 45 degrees) and model parameters were consistent across all runs. Grey boxes indicate the theorized range of impact velocity and remaining mass. See Section 4.1 for reference.

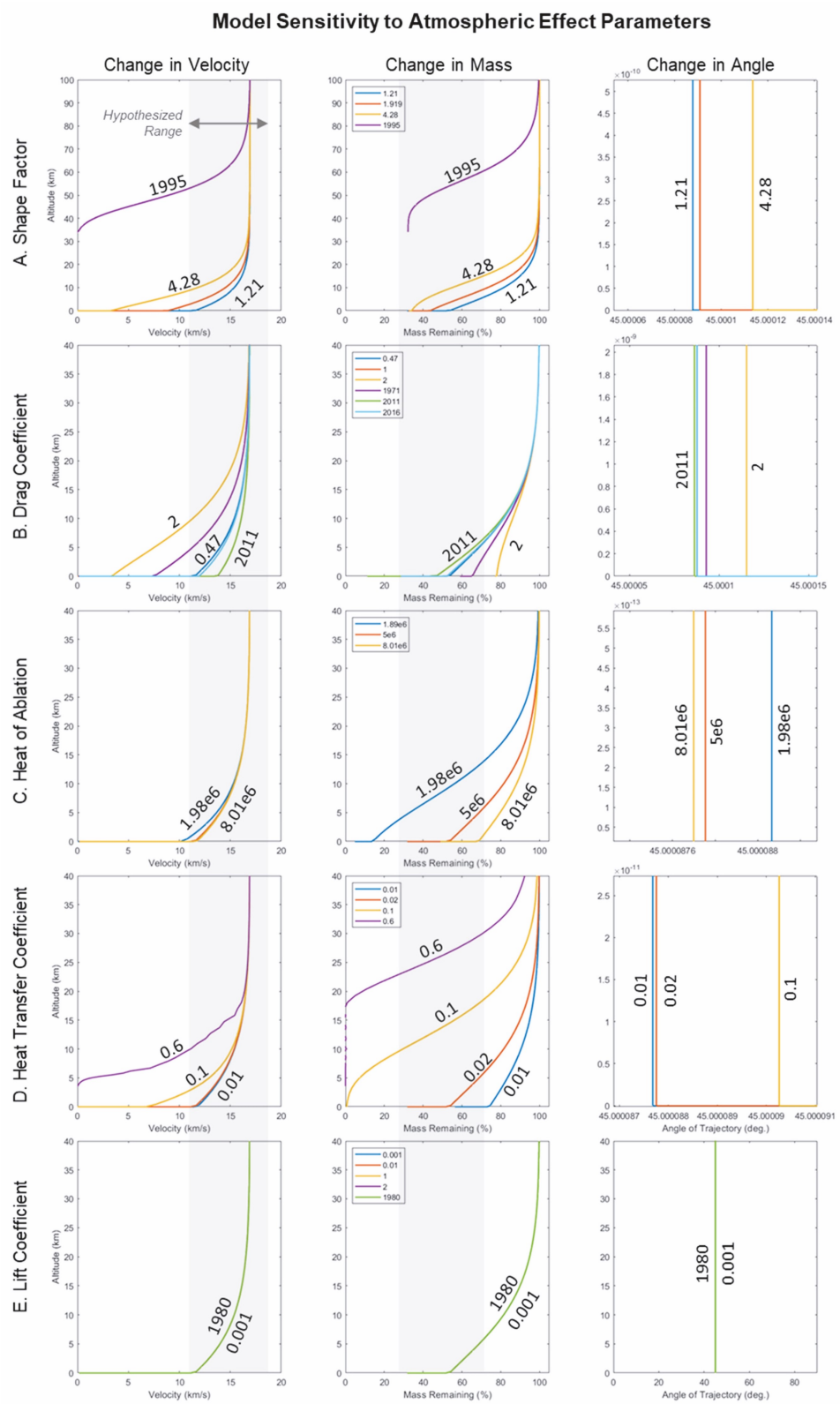


**Figure 5.** Model sensitivity to parameters. Variations in parameters for shape factor (A), drag coefficient (B), heat of ablation (C), heat transfer coefficient (D), and the lift coefficient (E) on the evolution of velocity (left), remaining mass (middle), and angle of trajectory (right) for a Meteor Crater-like projectile (50m in diameter, iron density (7,800 kg/m$^3$), 17 km/s, at 45 degrees) while model equations and other parameters remained consistent across all runs. Grey boxes indicate the theorized range of impact velocity and remaining mass. See Section 4.1 for reference.

The modeled Chelyabinsk meteor decreased in mass by 68 – 100% and decreased to a velocity of between ∼3 – 0 km/s; model results produced a crater between ∼160 – 0 m in diameter, with a depth between ∼35 – 0 m for runs with ablation only or ablation and fragmentation respectively. The modeled projectile began to fragment at the highest altitude (73 km) of the terrestrial analogs, exceeded the pancake limit at 50 km, lost ∼65% of its mass between 40 - 12 km, and dispersed until it burst at an altitude of 11.9 km. The real-world Chelyabinsk observations and models (Borovicka et al., 2013; Trigo-Rodríguez et al., 2021) show that the meteor started losing mass at 45 km, began a series of fragmentation events between 40 and 30 km, lost a significant amount of mass until 20 km, and entered dark flight at an altitude ∼17 km, producing a strewn field of meteorites and no crater (Borovicka et al., 2013).

The modeled Tunguska meteor decreased in mass by ∼47 – 67% and decreased to a velocity between ∼2 – 11 km/s; model results produced a crater between ∼410 – 839 m in diameter, with a depth between ∼86 – 182 m for runs with ablation only or ablation and fragmentation respectively. The modeled projectile slowly dispersed, exceeded the pancake limit of 5, and likely burst at an altitude of 11.3 km. The actual Tunguska meteor is hypothesized to have burst at an altitude of 5 – 10 km, which produced a shockwave at altitude and no discernible crater (Chyba et al., 1993).

### 4.3 Terrestrial Analogs on Venus and Mars

Terrestrial analogs for Chicxulub and Meteor Crater as well as the Tunguska and Chelyabinsk meteor were additionally run through AEM for Venus and Mars. Results (shown in Figure 8) show the Chicxulub impactor forming similarly sized craters on Venus (100 km), Earth (135 km), and Mars (150 km), along with the crater diameter formed by varying masses of surviving theoretical projectiles (20 km/s, 45°). The modeled Meteor Crater impactor did not survive Venusian atmospheric filtering but formed a crater on Earth (1.18 km) and Mars (2.07 km). The Tunguska meteor did not survive Venusian filtering but formed a crater on Earth (∼0.40 km) and Mars (1.45 km), however, the Tunguska impactor to Earth did exceed a pancake limit of 5, while it did not exceed a pancake limit of 5 for Mars. The modeled Chelyabinsk impactor did not survive filtering on Venus or Earth but did form a crater on Mars (∼600 m).

### 4.4 Projectile Survivability on Venus, Earth, and Mars

We used a theoretical projectile population, described in Section 3.6.3, to assess differences in the extent of filtering among the three atmospheres of Venus, Earth, and Mars. The evolution in deceleration and mass loss for a representative selection (n = 120 per target) of the 4,992 projectiles are shown with ablation and fragmentation in Figure 9. The Martian atmosphere yielded the smallest effect on projectiles, Earth's atmosphere moderately affected projectiles and Venus' atmosphere had the largest effect; the extent of atmospheric effects increased with the addition of fragmentation across all planets.

On average, significant deceleration and mass loss begins once the projectile reaches the stratosphere, at ∼50 km for Earth and 100 km for Venus, while Mars has little effect above 10 km. The Martian atmosphere allows all projectiles [1 m – 10 km] to impact the surface, while Earth allows some > 1 m, and Venus allows some > 60 m in diameter (Figure 10). The proportion of densities from chondritic, stony, stony-iron, and iron impactors are equal across Mars (25% each). On Earth, and more significantly on Venus, denser meteors are more likely to survive. For example, of the 1,565 impactors on Venus, 21% were chondritic and 31% were iron. The number of successful impactors with oblique angles [15° – 45°] is lower than projectiles with greater angles relative to horizontal for all planets, with the smallest proportion of impactors at 15° (Mars 13%, Earth 9%, Venus 7%). Mars allows the survival of all projectiles with velocities ≥ 15 km/s

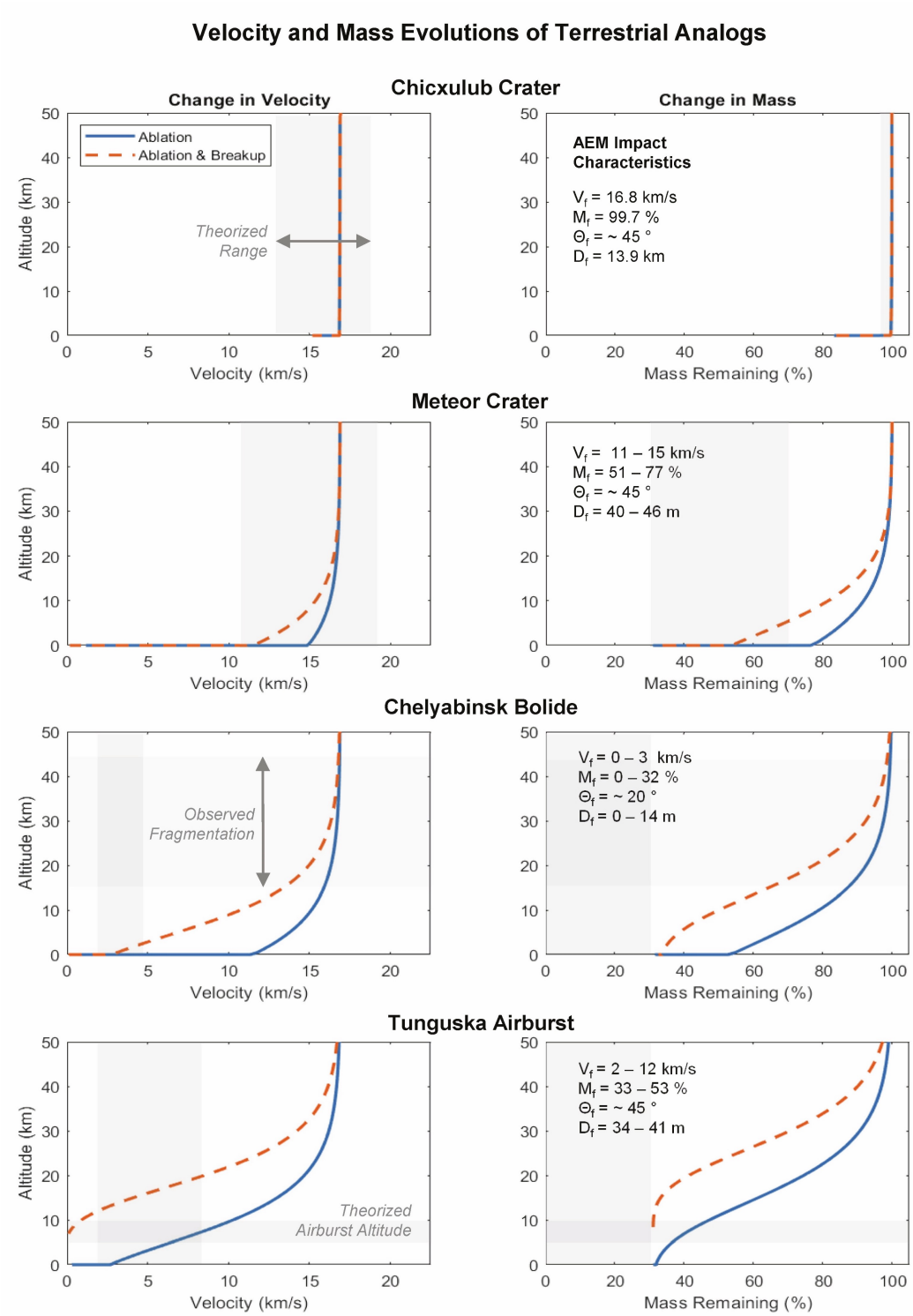


**Figure 6.** Modeled evolution of terrestrial analog velocities (left) and masses (right) during travel through Earth's atmosphere, for Chicxulub Crater (top row), Meteor Crater (second row), Chelyabinsk meteor (third row), and the Tunguska air burst (bottom row). Modeled velocity and mass evolution of projectiles are shown with ablation only (solid blue) and with ablation plus fragmentation (orange dashed). The range of final impact characteristics (ablation, ablation with breakup) is listed for each, along with grey boxes indicating the theorized range of impact velocity and remaining mass. See Section 4.2 for reference.

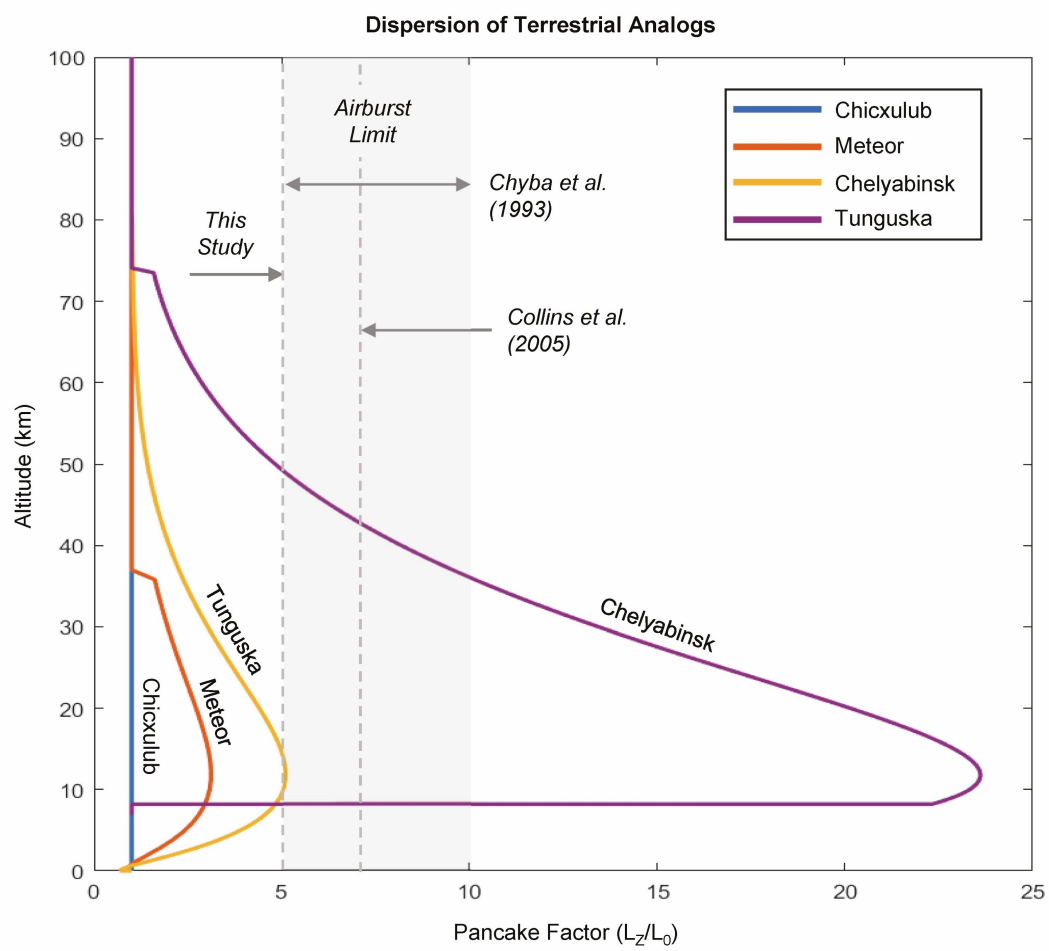


**Figure 7.** Dispersion of terrestrial analog fragments. The ratio of the pancaked diameter to the original projectile diameter at altitude for the terrestrial analog population; Chicxulub Crater (blue), Meteor Crater (red), Chelyabinsk (yellow), and Tunguska (purple). The limit of pancaking before airburst occurs of previous studies is shaded and marked with dashed lines. Grey box indicates a range of airburst limits. See Section 4.2 for reference.

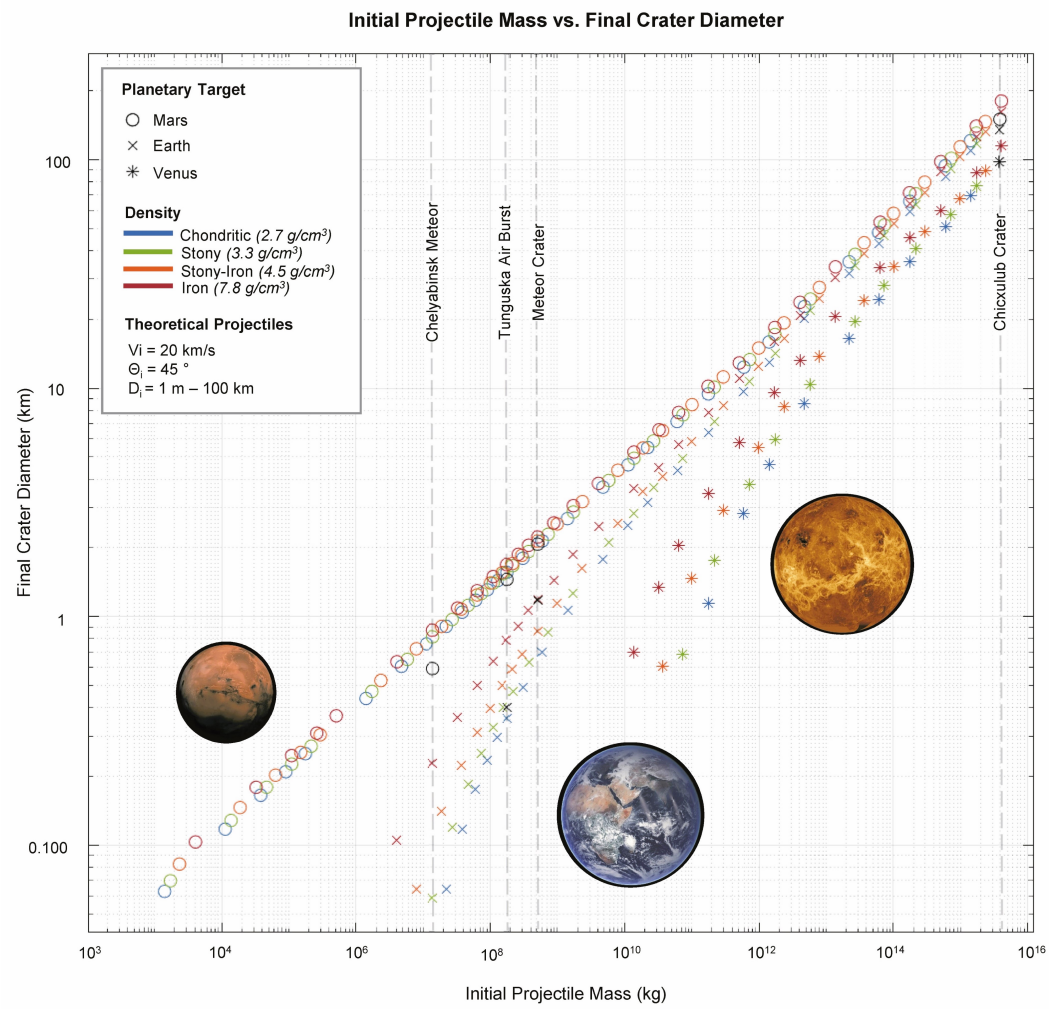


**Figure 8.** Initial projectile mass vs. final crater diameter for Venus, Earth, and Mars of terrestrial analogs and the theoretical population. Initial projectile diameters and masses with their respective final crater diameter for Mars (circle), Earth (x), and Venus (asterisk). Color corresponds to projectile type: iron (red), stony-iron (orange), stony (green), and chondritic (blue). All theoretical projectiles (n = 120 per target) have initial velocities of 20 km/s and angles of 45°. Dashed lines show the terrestrial analogs masses for Chicxulub and Meteor Crater, and the Tunguska and Chelyabinsk Meteors. See Section 4.3 for reference. Planetary images source: NASA. Note: this theoretical population (n = 120 per target) is expanded from the one described in Section 3.6.3 to also include projectiles with diameters of 2-5 m, to bridge an artificial gap between the masses of projectiles with a diameter of 1 and 10 m.

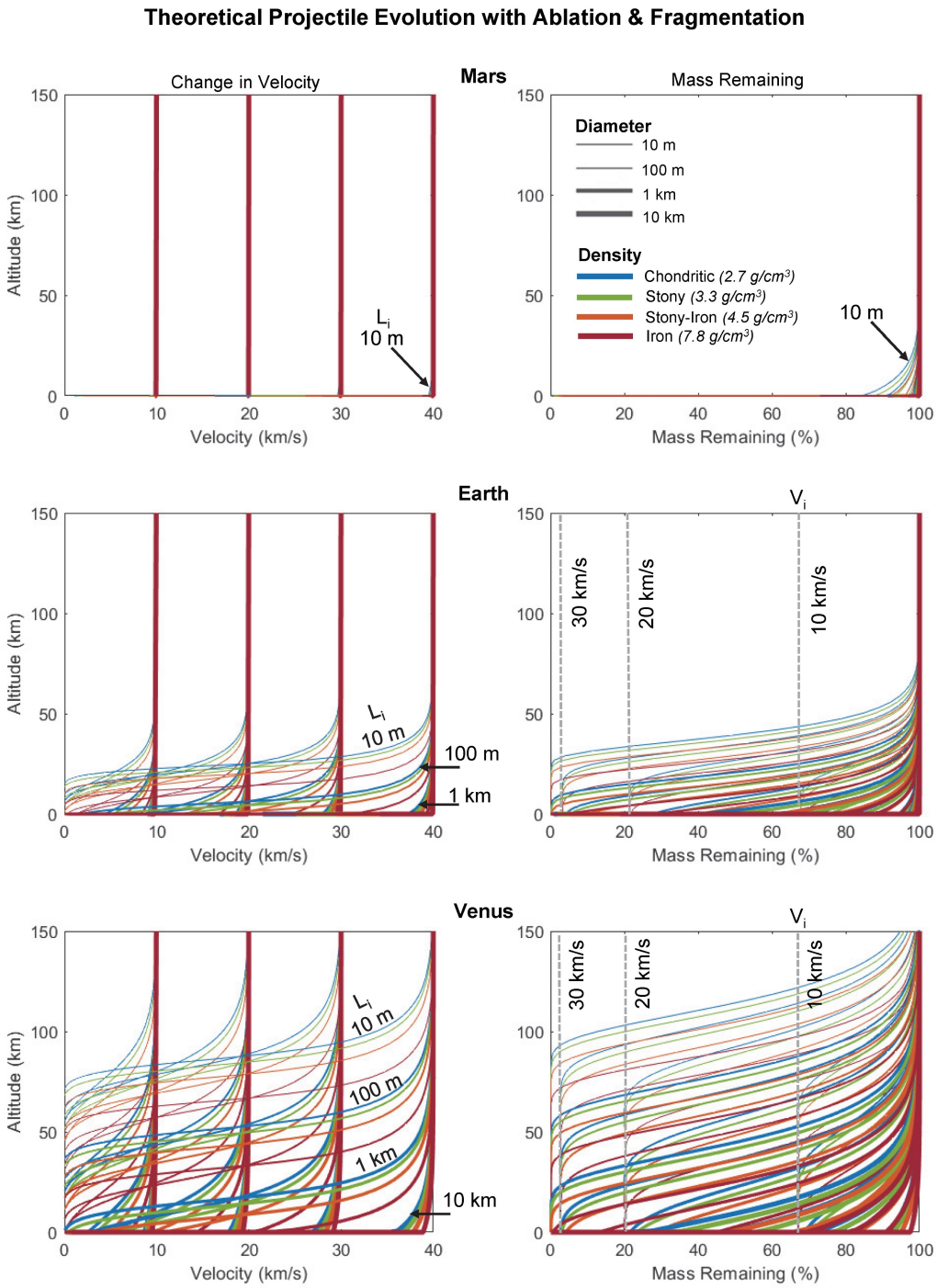


**Figure 9.** Projectile evolution of theoretical projectiles for Venus, Earth, and Mars, with ablation and fragmentation. Velocity (left) and mass remaining (right) at altitude for a selection of the theoretical projectile population (n = 64) through the atmospheres of Mars (top), Earth (middle), and Venus (bottom). Diameters vary between 10 m – 10 km, velocities vary between 10 to 40 km/s, and all projectiles have an initial angle of trajectory of 45 degrees. Vertical dashed lines on remaining mass plots denote the initial velocities (10, 20, 30 km/s) and the remaining mass of 10 and 100-m diameter projectiles that reached a velocity of 0 km/s and calculations ceased. See Section 4.4 for reference.

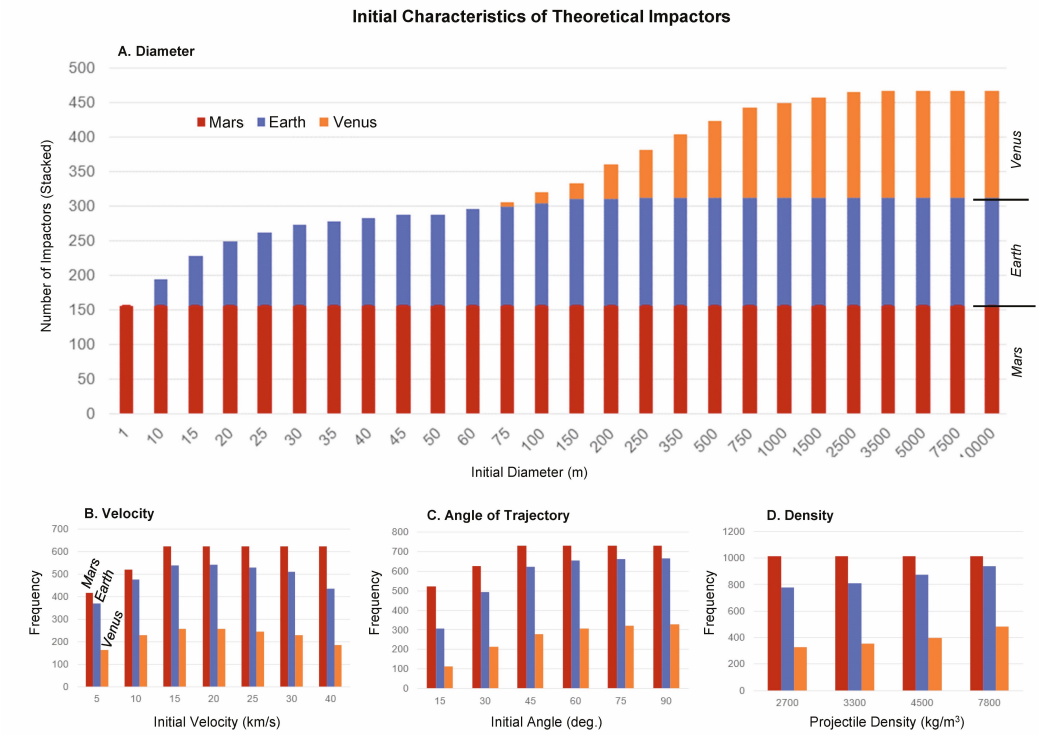


**Figure 10.** Initial characteristics of theoretical impactors (n = 4,992 per target) for Venus, Earth, and Mars. Initial characteristics of surviving projectiles with (A) showing a stacked bar plot of impactor frequency by diameter, and standard bar plots of (B) initial velocity, (C) initial angle of trajectory, (D) and density to impact the surface of Mars (red), Earth (blue), and Venus (orange). See Section 4.4 for reference.

in equal proportion, while Earth and Venus are normally distributed around 20 km/s with fewer impactors at lower and higher velocities.

Of the 4,992 possible projectiles assessed in the model, Mars filtered ∼19% both with ablation and with the addition of fragmentation, Earth filtered 23% and 32% respectively, and Venus filtered 49% and 69% respectively. The average impact characteristics, and crater statistics can be compared to determine the average effect of each atmosphere on the population. The density, diameter, and angle of impactors increased from Mars to Earth to Venus, while the impact velocity and percent mass retained decreased in a similar sequence. Comparably, the maximum diameter of crater formed on each planetary body decreased, in sequence, from the Moon to Mars, Earth, and Venus (Figure 10). With a dearth of smaller craters due to atmospheric filtering, the mean crater diameter increased from the Moon to Venus.

Model results show Mars, Earth, and Venus preferentially filter small, less dense projectiles (masses $< 10^3$ kg), lower angles of trajectory ($< 45°$), and those traveling at velocities lower than 10 km/s and greater than 30 km/s (Figure 8, Figure 10). Projectiles exceeded a pancake limit of 5 at altitudes between 7 – 16 km for Mars, 11 – 31 km for Earth, and 22 – 133 km for Venus, with the majority of airburst events occurring at the lower threshold. Airbursts at higher altitudes produced larger pancake factors up to 15 on Mars, 40 on Earth, and 120 on Venus and did not produce craters. Projectile mass and crater diameter were linearly related on both the Moon and Mars; however, the relationship decays exponentially below masses of $10^{12}$ kg on Earth and Venus, with

larger masses producing smaller craters comparatively. Figure 11 shows the range of crater diameters formed on the Moon, Mars, Earth, and Venus for all modeled initial angles, masses, velocities, and maximum pancake factors. Craters diameters at least 100 m, 1 km, and 10 km were formed by a minimum initial mass ranging across seven orders of magnitude on Mars ($10^3$, $10^6$, $10^{10}$ kg respectively), four orders of magnitude for Earth ($10^6$, $10^8$, $10^{11}$ kg respectively), and two orders of magnitude for Venus ($10^{10}$, $10^{11}$, and $10^{12}$ kg).

## 5 Discussion

There are three principal outcomes of this study. First, we have developed a new tool that we hope will be of strong use to the community. The Atmospheric Effects Model (AEM) simulates the atmospheric effects of mass loss, deceleration, and fragmentation on a user-defined population of projectiles, and estimates a corresponding population of impact craters for the projectiles that successfully strike the planet's surface. AEM aims to provide a user-friendly and modular tool to allow researchers a model that can be tuned to any study's specific projectile population, atmospheric and surface characteristics, as well as modeling methodologies, equations, and parameters.

Second, we have tested the sensitivity of potential impactors to many different equation and parameter choices, showing that impactor trajectories and crater formation are quite sensitive to some choices (e.g. heat coefficient) but less sensitive to others (e.g. lift coefficient). Preliminary results appear robust to most published equations and many variations are within reasonable ranges of projectile parameters. The greatest discrepancy in output results depending on the equations used were associated with the deceleration Equation 29 (Bronshten, 1983) and the mass loss Equation 31 (Campbell-Brown & Koschny, 2004). This is most likely due to the original purposes of these equations, as they are intended to calculate the evolution of micrometeorites and should not be used when modeling the evolution of larger meteoroids and asteroids. Thus, care should be taken that the appropriate equations are selected for a given projectile population. As equations and assumptions are chosen with a series of flag selections at the beginning of the script, the model currently cannot switch between algorithm options on the fly, e.g., using an asteroid ablation equation up until it is depleted to a micrometeorite scale and then switching to an ablation equation for micrometeorites. However, this modularity does showcase that AEM can be used on a variety of initial population sizes, at least when equations and assumptions are selected properly.

Third, the results of our simulations are broadly consistent with the current findings in projectile evolution and crater formation. The evolution of a projectile in AEM with particular characteristics and its probability of surviving atmospheric filtering align with the understanding of previous studies of atmospheric effects on deceleration and mass loss. For Earth, the majority of projectiles below 1 km in diameter decreased in mass between 30 – 70%, within range of expected values (Artemieva & Pierazzo, 2009; Johnston et al., 2018), the deceleration of projectiles with higher initial velocities was greater than those with lower velocities, and the majority of atmospheric effects occurred below at altitude of 30 km (Baldwin & Sheaffer, 1971). From this analysis, we found that AEM agrees with hypothesized terrestrial analog characteristics for large asteroids ($>$ 1 km) as well as relatively small (50 m) but high-density meteoroids. This broad agreement is likely due to the fact that larger and denser projectiles are not as significantly affected by ablation and fragmentation (Holsapple, 1993). Discrepancies between modeled and observed crater dimensions could be due to a number of factors, including differences in hypothesized initial projectile characteristics (e.g. Chicxulub) (Toon et al., 1997; Pierazzo & Melosh, 2000; Collins et al., 2005), differences in projectile and surface density (e.g. Meteor Crater) (Melosh & Collins, 2005; Artemieva & Pierazzo, 2009), or oversimplifications in the fragmentation of small projectiles (e.g. Chelyabinsk) (Borovicka et al., 2013; Robertson & Mathias, 2017; Flynn et al., 2018). Note that given the strong

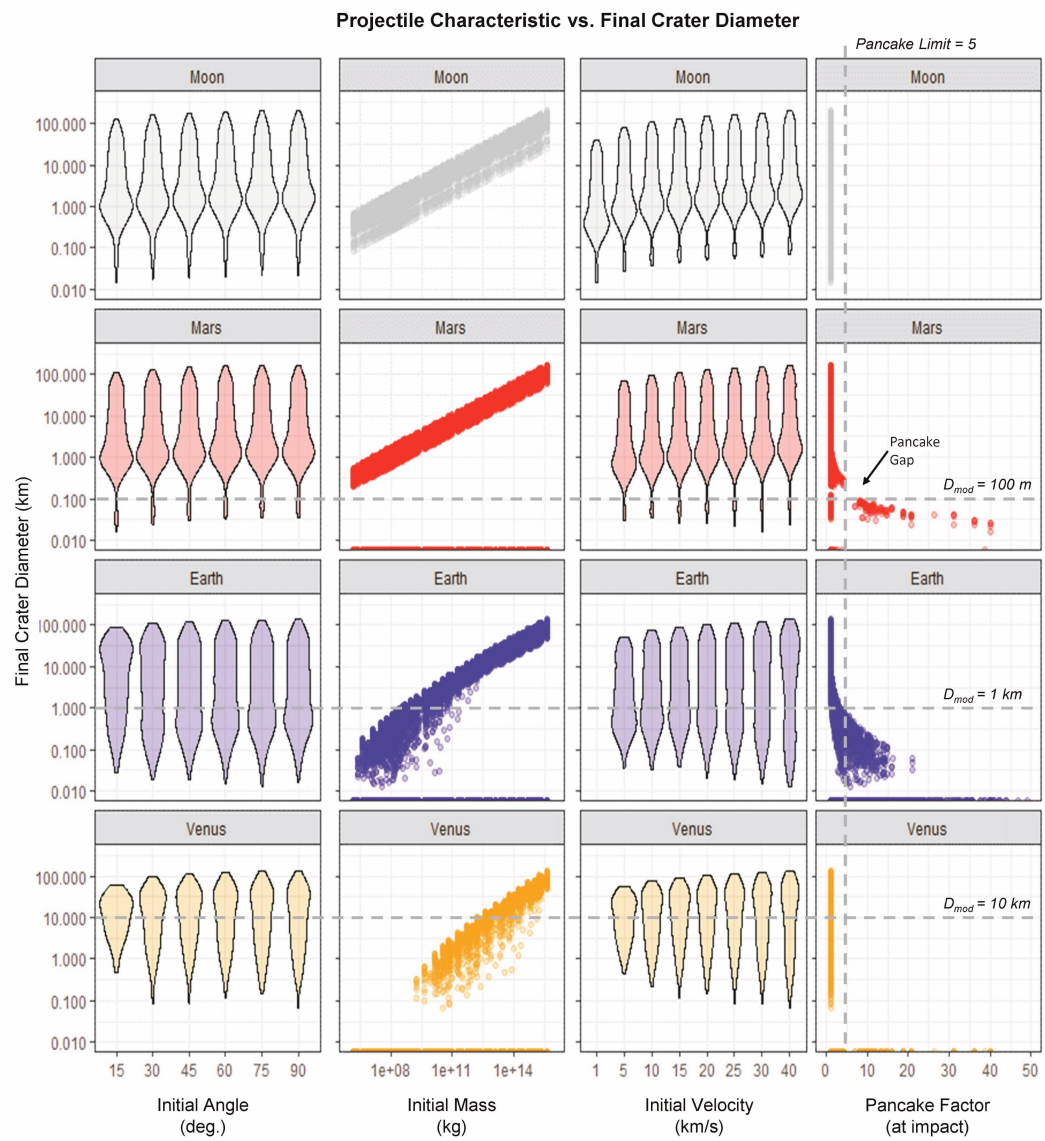


**Figure 11.** Initial projectile characteristics vs. final crater diameter for Venus, Earth, the Moon, and Mars. Initial projectile characteristics for angle (left), mass (middle left), velocity (middle right), and maximum pancake factor vs. final crater diameter on the Moon (top), Mars (second row), Earth (third row), and Venus (bottom). Violin plots show the relative frequency of each characteristic per crater diameter formed (n = 4,992 per target). Dashed lines show a pancake limit of 5 (vertical) and the projectile diameter threshold ($D_{mod}$) for ablation and breakup (horizontal). See Section 4.4 for reference.

dependence of fragmentation sequences on an individual meteor's internal composition and structure, it is not surprising that the output of AEM does not precisely match the observed fragmentation patterns for Chelyabinsk.

Comparing initial projectile characteristics against final crater diameters across the three planets, our results agree with previous studies on the effective filtering of small less-dense objects through atmospheres and constrains the magnitude and possible projectile characteristics (velocities, masses, angles, and fragment dispersion) with the potential to form craters. Mars and Earth show similar results with respect to distributions; however, Earth's atmospheric effects reduce projectile mass at a higher magnitude and thus allow for the creation of smaller craters when considering a limited population of projectiles. For Mars, using a projectile modification threshold at a diameter of 100 m (compared to 1 km for Earth), showed a gap in pancake factors exceeding 5 for crater diameters between 400 – 100 m. This result suggests that our current estimate of projectiles less than 100 m not being affected by the Martian atmosphere may be an underestimation and that the true value may be closer to 400 m.

In agreement with previous models and hypotheses (Tauber & Kirk, 1976; K. J. Zahnle, 1992; Herrick & Phillips, 1994; Korycansky & Zahnle, 2004), our results suggest that Venus's impactor population is likely skewed towards larger, denser objects, and the production of smaller craters ($< 1$ km) is rare. On average, the majority of atmospheric effects for Venus began at an altitude of $\sim$100 km, in agreement with McAuliffe and Christou (2006), who modeled the altitude of maximum brightness of micrometeorites between 90 – 120 km. This result reinforces that Venus affects projectiles at a much higher altitude than Earth, and thus has a larger capacity to inhibit and alter incoming projectiles. Results also show that craters up to 805 m could be formed by airbursts at altitudes between 21 – 23 km with a maximum pancake factor between 5 – 7 times the initial projectile diameter. This type of investigation could prove fruitful when constraining projectile characteristics likely to produce the distinctive crater clusters and airburst shadows on Venus.

Schaber et al. (1992) suggest that the Venusian atmosphere potentially filters 98% of projectiles that would form craters between 2 – 35 km in diameter and that projectile mass is the dominant characteristic when determining the potential of forming a crater on the surface. The results of this study are consistent with mass being the dominant characteristic determining the likelihood of a projectile surviving atmospheric filtering. Of the variables we examined, diameter (strongly related to mass) is the largest determining factor of crater size, followed by density, velocity, and then angle. Of the possible projectiles modeled in this study, nearly all below 60 m in diameter were filtered. Tauber and Kirk (1976) estimated the smallest craters on Venus to be on the order of 150 – 300 m; we show that this value may be lower at around 80 m in diameter. Recent 2D and 3D hydrodynamic modeling of Venusian atmospheric effects (Korycansky et al., 2000, 2002; Korycansky & Zahnle, 2003, 2004, 2005) have constrained impactors to have initial masses $> 10^{12}$ kg yielding a surface age of 730 $\pm$ 110 Ma; we show that minimum masses able to withstand atmospheric filtering may actually be lower than originally thought at $10^{10}$ kg.

Finally, there are some important limitations to our study. We assumed projectiles to be homogenous spheres with no void spaces or zones of weakness. Projectile masses, diameters, and radii are calculated with simple spherical equations incorporating a bulk density. However, observations (Britt & G. J. Consolmagno, 2003; Flynn et al., 2018) and recent findings from asteroid flyby and sample collection missions (Lauretta et al., 2019; Elkins−Tanton et al., 2020), show that this assumption is far from the truth. Meteors are often irregularly shaped, with varying levels of porosity and surfaces consisting of unconsolidated rocky material. These variations in shape put inherent constraints on what shape factors and drag coefficients should be used or calculated in the atmospheric effects model. Additionally, the type of projectile, either of chondritic, stony, or iron-like material, also imparts certain considerations on the heat transfer coefficient and

the heat of ablation assumptions that are used. For example, our results for variations in the heat of ablation yielded the largest effect on model outputs. We assumed this value to be constant for all densities; however, it should ideally be constrained to the individual projectile, as different meteorite types have varying heat capacities and thermal conductivities.

Meteor fragmentation and dispersion, which has been the subject of experimentation with over decades of modeling studies, remains challenging to simulate. Fragmentation has been modeled using mechanical (Baldwin & Sheaffer, 1971; Passey & Melosh, 1980) and hydrodynamical methodologies (Ivanov et al., 1997; Korycansky & Zahnle, 2005). Both have advantages and disadvantages, hydrodynamic models provided more realistic approximations at times but with highly variable results with the incorporation of random chance (V. Shuvalov & Artemieva, 2002; Korycansky & Zahnle, 2005; Artemieva & Pierazzo, 2009). The process of fragmentation occurs when the stagnation pressure exerted onto the frontal area exceeds the yield strength, which can happen at different altitudes and results in dissolution into different number of fragments depending on the unique features of the projectile itself. While the method for determining the stagnation pressure is generally agreed upon (Passey & Melosh, 1980), the number of fragments a projectile will break into varies across methodologies. Baldwin and Sheaffer (1971) modeled fragmentation to an exponential form, yielding thousands of fragments, while Korycansky and Zahnle (2005) modeled using a random number (determined by a random number generator) of fragments between $2 - 7$. Meteor fragmentation and dispersion is an area of high uncertainty that would benefit from future work.

A common assumption is that the projectile fragments at the altitude at which stagnation pressure is exceeded, and then the fragments are laterally dispersed (pancaking) with a transverse velocity. If the fragments disperse far enough away from the original body, exceeding the pancaking factor (Robertson & Mathias, 2017; Johnston et al., 2018), they can then be modeled as individual projectiles with the potential to form multi-floored craters (if close enough in proximity) or crater fields (if dispersed far enough). For simplicity, our mechanical model assumes that when the yield strength is exceeded, the projectile will add one additional fragment. This simplified model takes into account that over our time step intervals (a tenth of a second) the yield strength, once exceeded, is generally going to be exceeded in every time step thereafter. We acknowledge that this is not the most realistic manner of fragmentation and further investigations into fragmentation processes should be explored within this model.

## 6 Conclusion

This study introduces the Atmospheric Effects Model (AEM), a modular and user-friendly MATLAB script, which offers a straightforward approach to estimating the evolution of projectile populations in different atmospheres and the corresponding primary crater populations. Although this study focuses on the basic aspects of projectile evolution (deceleration, mass loss, and fragmentation) and crater morphology (simple and complex), AEM's modularity allows for future investigations to incorporate additional features such as the formation of strewn crater fields, secondary craters, and the process of crater erasure due to overprinting. Furthermore, in conjunction with 2D and 3D impact crater production models, AEM opens up possibilities for more comprehensive studies on the correlations between projectile populations, atmospheric filtering, and crater production.

The comparison of model results obtained using various numerical atmospheric effect equations and assumptions show a general agreement in terms of projectile evolution. However, caution should be taken when choosing the equation and associated parameters related to changes in mass over time, as the projectile evolution can exhibit substantial variations in the duration and extent of mass loss depending on these choices.

This finding highlights the importance of future studies to consider which numerical equations and assumptions are representative of model parameters most appropriate in different circumstances.

Model results show that, based on current atmospheric profiles, the minimum projectile masses required to form craters > 1 km differ for Venus, Earth, and Mars. On Mars, a mass of at least $10^6$ kg is required, while on Earth, the threshold increases to $10^8$ kg, and on Venus, an even greater mass of $10^{11}$ kg is required. These findings emphasize the substantial influence of a planet's atmospheric conditions on the formation of craters, highlighting the need for tailored investigations and considerations when studying projectile populations to and impact craters on different terrestrial planets.

## 7 Open Research

**Acknowledgments**

We thank the University of North Carolina's Department of Earth, Marine and Environmental Sciences' Martin Research Fellowship, as well as James Madison University's Jeffrey E. Tickle Family Endowment in Science and Mathematics and Department of Geology and Environmental Science's Doherty Geology Student Research Endowment for funding this research. This work would not have been possible without the support of Hunter Hughes, the American Geophysical Union 2021 OSPA Planetary Science judges, and many others. Thank you.

### Data Availability

The MATLAB scripts for AEM (Atmospheric Effects Model) and FLAVRS (AEM Projectile Population Builder), projectile population matrices, figures, and original data presented in the study can be found in the following GitHub repository linked below. Further inquiries and requests for larger files (e.g., model run workspaces) can be directed to the corresponding author.

Repository link: `https://github.com/mjdudek/AEM_Hughes_2024`

## References

Artemieva, N., & Pierazzo, E. (2009). The canyon diablo impact event: Projectile motion through the atmosphere [Journal Article]. *Meteoritics & Planetary Science*, *44*(1), 25-42. doi: 10.1111/j.1945-5100.2009.tb00715.x

Artemieva, N., & Shuvalov, V. (1996). Interaction of shock waves during the passage of a disrupted meteoroid through the atmosphere [Journal Article]. *Shock waves*, *5*(6), 359-367.

Artemieva, N., & Shuvalov, V. (2001). Motion of a fragmented meteoroid through the planetary atmosphere [Journal Article]. *Journal of Geophysical Research: Planets*, *106*(E2), 3297-3309. doi: 10.1029/2000je001264

Aziz, E., Chassapis, C., Esche, S., Dai, S., Xu, S., & Jia, R. (2008). Online wind tunnel laboratory [Conference Proceedings]. In *Annual conference & exposition proceedings.* ASEE Conferences. doi: 10.18260/1-2--3402

Baldwin, B., & Sheaffer, Y. (1971). Ablation and breakup of large meteoroids during atmospheric entry [Journal Article]. *Journal of Geophysical Research*, *76*(19), 4653-4668. doi: 10.1029/ja076i019p04653

Bland, P. A., & Artemieva, N. A. (2003). Efficient disruption of small asteroids by earth's atmosphere [Journal Article]. *Nature*, *424*(6946), 288-291. doi: 10.1038/nature01757

Borovicka, J., Spurný, P., Brown, P., Wiegert, P., Kalenda, P., Clark, D., &

Shrbený, L. (2013). The trajectory, structure and origin of the chelyabinsk asteroidal impactor [Journal Article]. *Nature*, *503*(7475), 235-237.

Britt, D. T., & G. J. Consolmagno, S. J. (2003). Stony meteorite porosities and densities: A review of the data through 2001 [Journal Article]. *Meteoritics & Planetary Science*, *38*(8), 1161-1180. doi: 10.1111/j.1945-5100.2003.tb00305.x

Bronshten, V. A. (1983). *Physics of meteoric phenomena* [Book]. D. Reidel Publishing Comapny.

Campbell-Brown, M. D., & Koschny, D. (2004). Model of the ablation of faint meteors [Journal Article]. *Astronomy & Astrophysics*, *418*(2), 751-758. doi: 10.1051/0004-6361:20041001-1

Ceplecha, Z., & Revelle, D. O. (2005). Fragmentation model of meteoroid motion, mass loss, and radiation in the atmosphere [Journal Article]. *Meteoritics & Planetary Science*, *40*(1), 35-54. doi: 10.1111/j.1945-5100.2005.tb00363.x

Christensen, N. I., & Mooney, W. D. (1995). Seismic velocity structure and composition of the continental crust: A global view [Journal Article]. *Journal of Geophysical Research: Solid Earth*, *100*(B6), 9761-9788. doi: 10.1029/95JB00259

Chyba, C. F., Thomas, P. J., & Zahnle, K. J. (1993). The 1908 tunguska explosion: atmospheric disruption of a stony asteroid [Journal Article]. *Nature*, *361*(6407), 40-44. doi: 10.1038/361040a0

Collins, G. S., Melosh, H. J., & Marcus, R. A. (2005). Earth impact effects program: A web-based computer program for calculating the regional environmental consequences of a meteoroid impact on earth [Journal Article]. *Meteoritics & Planetary Science*, *40*(6), 817-840. doi: 10.1111/j.1945-5100.2005.tb00157.x

Durand-Manterola, H. J., & Cordero-Tercero, G. (2014, March 01, 2014). *Assessments of the energy, mass and size of the chicxulub impactor* [Electronic Article].

Elkins−Tanton, L. T., Asphaug, E., Bell, J. F., Bercovici, H., Bills, B., Binzel, R., ... Marchi, S. (2020). Observations, meteorites, and models: a preflight assessment of the composition and formation of (16) psyche [Journal Article]. *Journal of Geophysical Research: Planets*, *125*(3), e2019JE006296.

Fassett, C. I. (2016). Analysis of impact crater populations and the geochronology of planetary surfaces in the inner solar system [Journal Article]. *Journal of Geophysical Research: Planets*, *121*(10), 1900-1926. doi: 10.1002/2016je005094

Flynn, G. J., Consolmagno, G. J., Brown, P., & Macke, R. J. (2018). Physical properties of the stone meteorites: Implications for the properties of their parent bodies [Journal Article]. *Geochemistry*, *78*(3), 269-298. doi: 10.1016/j.chemer.2017.04.002

Herrick, R. R., & Phillips, R. J. (1994). Effects of the venusian atmosphere on incoming meteoroids and the impact crater population [Journal Article]. *Icarus*, *112*(1), 253-281. doi: 10.1006/icar.1994.1180

Hoerner, S. F. (1965). *Fluid dynamic drag: Practical information on aerodynamic drag and hydrodynamic resistance* (Second ed.) [Book]. Author

Holsapple, K. A. (1993). The scaling of impact processes in planetary sciences [Journal Article]. *Annual Review of Earth and Planetary Sciences*, *21*(1), 333-373. doi: 10.1146/annurev.ea.21.050193.002001

Hughes, D. W. (1993). Meteorite incidence angles [Journal Article]. *Journal of the British Astronomical Association*, *103*, 123-126.

Humes, D. H., & Bess, T. D. (1972). *Nasa report: Meteoroid impacts on mars and the secondary particle environment* (Report No. N72-33829).

Ivanov, B. A. (2008). Size-frequency distribution of asteroids and impact craters: Estimates of impact rate [Journal Article]. *Catastrophic Events Caused by Cosmic Objects*. doi: 10.1007/978-1-4020-6452-4_2

Ivanov, B. A., Deniem, D., & Neukum, G. (1997). Implementation of dynamic strength models into 2d hydrocodes: Applications for atmospheric breakup and impact cratering [Journal Article]. *International Journal of Impact Engineer-*

*ing*, *20*(1-5), 411-430. doi: 10.1016/s0734-743x(97)87511-2

Ivanov, B. A., Nemchinov, I. V., Svetsov, V. A., Provalov, A. A., Khazins, V. M., & Phillips, R. J. (1992). Impact cratering on venus: Physical and mechanical models [Journal Article]. *Journal of Geophysical Research*, *97*(E10), 16167. doi: 10.1029/92je01633

Johnston, C. O., Stern, E. C., & Wheeler, L. F. (2018). Radiative heating of large meteoroids during atmospheric entry [Journal Article]. *Icarus*, *309*, 25-44. doi: 10.1016/j.icarus.2018.02.026

Khanukaeva, D. Y. (2003). On the coefficients in meteor physics equations [Conference Proceedings]. In *Aip conference proceedings.* AIP. doi: 10.1063/1.1581615

Korycansky, D. G., & Zahnle, K. J. (2003). High-resolution simulations of the impacts of asteroids into the venusian atmosphere iii: further 3d models [Journal Article]. *Icarus*, *161*(2), 244-261. doi: 10.1016/s0019-1035(02)00049-0

Korycansky, D. G., & Zahnle, K. J. (2004). Atmospheric impacts, fragmentation, and small craters on venus [Journal Article]. *Icarus*, *169*(2), 287-299. doi: 10.1016/j.icarus.2004.01.010

Korycansky, D. G., & Zahnle, K. J. (2005). Modeling crater populations on venus and titan [Journal Article]. *Planetary and Space Science*, *53*(7), 695-710. doi: 10.1016/j.pss.2005.03.002

Korycansky, D. G., Zahnle, K. J., & Mac Law, M. (2000). High-resolution calculations of asteroid impacts into the venusian atmosphere [Journal Article]. *Icarus*, *146*(2), 387-403.

Korycansky, D. G., Zahnle, K. J., & Mac Low, M. M. (2002). High-resolution simulations of the impacts of asteroids into the venusian atmosphere ii: 3d models [Journal Article]. *Icarus*, *157*(1), 1-23. doi: 10.1006/icar.2002.6795

Lauretta, D. S., Hergenrother, C. W., Chesley, S. R., Leonard, J. M., Pelgrift, J. Y., Adam, C. D., ... Becker, K. J. (2019). Episodes of particle ejection from the surface of the active asteroid (101955) bennu [Journal Article]. *Science*, *366*(6470), eaay3544.

Mac Low, M. M., & Zahnle, K. (1994). Explosion of comet shoemaker-levy 9 on entry into the jovian atmosphere [Journal Article]. *Astrophys J*, *434*(1), L33-6. (Mac Low, M M Zahnle, K Journal Article Research Support, U.S. Gov't, Non-P.H.S. United States 1994/10/10 Astrophys J. 1994 Oct 10;434(1):L33-6. doi: 10.1086/187565.) doi: 10.1086/187565

McAuliffe, J., & Christou, A. (2006). Modelling meteor ablation in the venusian atmosphere [Journal Article]. *Icarus*, *180*(1), 8-22. doi: 10.1016/j.icarus.2005.07.012

Melosh, H. J. (1981). Atmospheric breakup of terrestrial impactors [Conference Proceedings]. In *Lunar and planetary science conference* (p. 29-35). New York and Oxford, Pergamon Press.

Melosh, H. J. (2011). *Planetary surface processes: 6. impact cratering* [Book]. Cambridge, UK ; New York: Cambridge University Press. (2011019269 H. Jay Melosh. 26 cm. Includes bibliographical references and index. Machine generated contents note: Preface; 1. The grand tour; 2. The shapes of planets and moons; 3. Strength versus gravity; 4. Tectonics; 5. Volcanism; 6. Impact cratering; 7. Regoliths, weathering and surface texture; 8. Slopes and mass movement; 9. Wind; 10. Water; 11. Ice; References; Index. Cambridge planetary science series.)

Melosh, H. J., & Collins, G. S. (2005). Meteor crater formed by low-velocity impact [Journal Article]. *Nature*, *434*(7030), 157-157. doi: 10.1038/434157a

Melosh, H. J., & Vickery, A. M. (1989). Impact erosion of the primordial atmosphere of mars [Journal Article]. *Nature*, *338*(6215), 487-489. doi: 10.1038/338487a0

Michel, P., & Morbidelli, A. (2007). Review of the population of impactors and the impact cratering rate in the inner solar system [Journal Article]. *Meteoritics &*

*Planetary Science*, *42*(11), 1861-1869. (OA status: bronze) doi: 10.1111/j.1945-5100.2007.tb00545.x

Moilanen, J., Gritsevich, M., & Lyytinen, E. (2021). Determination of strewn fields for meteorite falls [Journal Article]. *Monthly Notices of the Royal Astronomical Society*, *503*. doi: 10.1093/mnras/stab586

Morrison, F. A. (2013). *An introduction to fluid mechanics* [Book]. Cambridge University Press.

Naganna, S. R., Deka, P. C., Ch, S., & Hansen, W. F. (2017). Factors influencing streambed hydraulic conductivity and their implications on stream–aquifer interaction: a conceptual review [Journal Article]. *Environmental Science and Pollution Research*, *24*, 24765–24789. doi: 10.1007/s11356-017-0393-4

Neukum, G., Ivanov, B., & Hartmann, W. (2001). Crating records in the inner solar system in relation to the lunar reference system [Journal Article]. *Space Science Reviews*, *96*(1/4), 55-86. doi: 10.1023/a:1011989004263

Nicol, E. J., Macfarlane, J., & Hawkes, R. (1985). Residual mass from atmospheric ablation of small meteoroids [Journal Article]. *Planetary and Space Science*, *33*(3), 315-320. doi: 10.1016/0032-0633(85)90063-7

NOAA, U., NASA. (1976). *Resport: U.s. standard atmosphere* (Report).

Opik, E. J. (1958). *Physics of meteor flight in the atmosphere* [Book]. Courier Corporation.

Passey, Q. R., & Melosh, H. J. (1980). Effects of atmospheric breakup on crater field formation [Journal Article]. *Icarus*, *42*(2), 211-233. doi: 10.1016/0019-1035(80)90072-x

Phillips, R. J., Raubertas, R. F., Arvidson, R. E., Sarkar, I. C., Herrick, R. R., Izenberg, N., & Grimm, R. E. (1992). Impact craters and venus resurfacing history [Journal Article]. *Journal of Geophysical Research*, *97*(E10), 15923. doi: 10.1029/92je01696

Pierazzo, E., & Melosh, H. J. (2000). Understanding oblique impacts from experiments, observations, and modeling [Journal Article]. *Annual Review of Earth and Planetary Sciences*, *28*(1), 141-167. doi: 10.1146/annurev.earth.28.1.141

Popova, O. P., Jenniskens, P., Emel'yanenko, V., Kartashova, A., Biryukov, E., Khaibrakhmanov, S., ... (the Chelyabinsk Airburst Consortium) (2013). Chelyabinsk airburst, damage assessment, meteorite recovery, and characterization [Journal Article]. *Science*, *342*(6162), 1069-1073. doi: 10.1126/science.1242642

Ramanan, R. V., R.Pillai, J., & John, A. (2013). Design and analysis tool for mars atmospheric entry missions [Journal Article]. *International Journal of Aerospace Innovations*, *Volume 5*, pp.29-40. doi: 10.1260/1757-2258.5.1.29

Robertson, D. K., & Mathias, D. L. (2017). Effect of yield curves and porous crush on hydrocode simulations of asteroid airburst [Journal Article]. *Journal of Geophysical Research: Planets*, *122*(3), 599-613. doi: 10.1002/2016je005194

Schaber, G. G., Strom, R. G., Moore, H. J., Soderblom, L. A., Kirk, R. L., Chadwick, D. J., ... Russell, J. (1992). Geology and distribution of impact craters on venus: What are they telling us? [Journal Article]. *Journal of Geophysical Research: Planets*, *97*(E8), 13257-13301. doi: 10.1029/92JE01246

Schultz, P. H. (1992). Atmospheric effects on cratering efficiency [Journal Article]. *Journal of Geophysical Research: Planets*, *97*(E1), 975-1005.

Shuvalov, V. (1999). Multi-dimensional hydrodynamic code sova for interfacial flows: Application to the thermal layer effect [Journal Article]. *Shock Waves*, *9*(6), 381-390. doi: 10.1007/s001930050168

Shuvalov, V., & Artemieva, N. (2002). Numerical modeling of tunguska-like impacts [Journal Article]. *Planetary and Space Science*, *50*(2), 181-192.

Shuvalov, V. V., Artem'Eva, N. A., & Kosarev, I. B. (1999). 3d hydrodynamic code sova for multimaterial flows, application to shoemakerlevy 9 comet impact problem [Journal Article]. *International Journal of Impact Engineering*, *23*(1),

847-858.

Shuvalov, V. V., & Trubetskaya, I. A. (2010). The influence of internal friction on the deformation of a damaged meteoroid [Journal Article]. *Solar System Research*, *44*(2), 104-109. doi: 10.1134/s0038094610020036

Stevenson, D. J. (1987). Origin of the moon-the collision hypothesis [Journal Article]. *Annual Review of Earth and Planetary Sciences*, *15*(1), 271-315. doi: 10.1146/annurev.ea.15.050187.001415

Stoffler, D. (2006). Cratering history and lunar chronology [Journal Article]. *Reviews in Mineralogy and Geochemistry*, *60*(1), 519-596. doi: 10.2138/rmg.2006.60.05

Svetsov, V. V., Nemtchinov, I. V., & Teterev, A. V. (1995). Disintegration of large meteoroids in earth's atmosphere: Theoretical models [Journal Article]. *Icarus*, *116*(1), 131-153. doi: 10.1006/icar.1995.1116

Tauber, M. E., & Kirk, D. B. (1976). Impact craters on venus [Journal Article]. *Icarus*, *28*(3), 351-357. doi: 10.1016/0019-1035(76)90148-2

Taylor, F. W., Svedhem, H., & Head, J. W. (2018). Venus: The atmosphere, climate, surface, interior and near-space environment of an earth-like planet [Journal Article]. *Space Science Reviews*, *214*(1). doi: 10.1007/s11214-018-0467-8

Toon, O. B., Zahnle, K., Morrison, D., Turco, R. P., & Covey, C. (1997). Environmental perturbations caused by the impacts of asteroids and comets [Journal Article]. *Reviews of Geophysics*, *35*(1), 41-78. doi: 10.1029/96rg03038

Trigo-Rodríguez, J. M., Dergham, J., Gritsevich, M., Lyytinen, E., Silber, E. A., & Williams, I. P. (2021). A numerical approach to study ablation of large bolides: Application to chelyabinsk [Journal Article]. *Advances in Astronomy*, *2021*, 1-13. doi: 10.1155/2021/8852772

Turchak, L. I., & Gritsevich, M. I. (2014). Meteoroids interaction with the earth atmosphere [Journal Article]. *Journal of Theoretical and Applied Mechanics*, *44*(4), 15-28.

Vogel, M. (2020). Meteoroids: sources of meteors on earth and beyond [Journal Article]. *Contemporary Physics*, *61*(1), 54-55. doi: 10.1080/00107514.2020.1736170

Zahnle, K., & Mac Low, M. M. (1994). The collision of jupiter and comet shoemaker-levy 9 [Journal Article]. *Icarus*, *108*, 1-17. (Zahnle, K Mac Low, M M Journal Article Research Support, U.S. Gov't, Non-P.H.S. United States 1994/01/01 Icarus. 1994;108:1-17. doi: 10.1006/icar.1994.1038.) doi: 10.1006/icar.1994.1038

Zahnle, K. J. (1992). Airburst origin of dark shadows on venus [Journal Article]. *Journal of Geophysical Research*, *97*(E6), 10243. doi: 10.1029/92je00787